YALE
PEABODY
MUSEUM

P.O. BOX 208118 | NEW HAVEN CT 06520-8118 USA | PEABODY.YALE. EDU

## JOURNAL OF MARINE RESEARCH

The *Journal of Marine Research,* one of the oldest journals in American marine science, published important peer-reviewed original research on a broad array of topics in physical, biological, and chemical oceanography vital to the academic oceanographic community in the long and rich tradition of the Sears Foundation for Marine Research at Yale University.

An archive of all issues from 1937 to 2021 (Volume 1–79) are available through EliScholar, a digital platform for scholarly publishing provided by Yale University Library at https://elischolar.library.yale.edu/.

Requests for permission to clear rights for use of this content should be directed to the authors, their estates, or other representatives. The *Journal of Marine Research* has no contact information beyond the affiliations listed in the published articles. We ask that you provide attribution to the *Journal of Marine Research*.

Yale University provides access to these materials for educational and research purposes only. Copyright or other proprietary rights to content contained in this document may be held by individuals or entities other than, or in addition to, Yale University. You are solely responsible for determining the ownership of the copyright, and for obtaining permission for your intended use. Yale University makes no warranty that your distribution, reproduction, or other use of these materials will not infringe the rights of third parties.


This work is licensed under a Creative Commons Attribution-NonCommercial-ShareAlike 4.0 International License.
https://creativecommons.org/licenses/by-nc-sa/4.0/

*Journal of Marine Research, 64,* 1–42, 2006

# Generalized inversion of the Gent-Cane model of the tropical Pacific with Tropical Atmosphere-Ocean (TAO) data

**by A. F. Bennett[1,2], B. S. Chua[1], H.-E. Ngodock[3], D. E. Harrison[4] and M. J. McPhaden[4]**

ABSTRACT

We here describe the results of our latest effort to reanalyze TAO monthly mean surface and subsurface temperature observations constrained by a tropical Pacific ocean model, and simultaneously to evaluate the physical consistency of the observations and the model. Both tasks are executed by weak–constraint, four–dimensional variational assimilation of the observations into the model. In this study our reanalysis employs the reduced–gravity Gent–Cane model, combined with the 'KPP–interior' parameterization of vertical turbulent fluxes. With the limited vertical resolution adopted in previous studies of this model, the 'W4DVAR' or inverse method fails to produce an acceptable reanalysis, as the dynamical residuals are too large locally in space and time. Moreover, the objective significance test that is an essential product of the inversion rejects the model, even though the model is imposed only as a weak constraint, as convincingly as the even simpler Zebiak–Cane model was rejected (Bennett *et al.*, 1998, 2000). In order to obtain a locally plausible reanalysis of the observations, we have to employ significantly finer vertical resolution. The calculations are extremely expensive and technically difficult; in the interests of efficiency and convergence, we solve the fixed–interval smoothing problem for 3–month intervals (during the 1997–1998 El Niño, December 1996–March 1998), and we impose the continuity equations for layer thickness as strong constraints. We present detailed results for just one such experiment which shows the model in the best light. The resulting fits to the monthly-mean data are within our prior error assumptions and so constitute a highly plausible reanalysis. However, the significance test statistic for the inversion exceeds its expected value by many tens of standard deviations, forcing us to the inference that the model cannot in fact be reconciled with the observations. The paradox of locally small residuals and a large test statistic is explained by an analysis of the degrees of freedom allowed in the weak constraints.

## 1. Introduction

The TAO array (McPhaden, 1995) is collecting real-time measurements of tropical Pacific surface winds, subsurface temperatures and equatorial Pacific subsurface currents. The regularity of these data provides an opportunity to test ocean models in a rigorously objective

1. College of Oceanic and Atmospheric Sciences, Oregon State University, Corvallis, Oregon, 97331, U.S.A.
2. Corresponding author. ***email: bennett@coas.oregonstate.edu***
3. Department of Marine Science, University of Southern Mississippi, Stennis Space Center, Mississippi, 39529, U.S.A.
4. NOAA/PMEL, 7600 Sand Point Way, Seattle, Washington, 98115, U.S.A.

fashion, with the models expressed as a formal hypothesis. The tests are conceptually simple, being no more than least-squares regression with additional chi–squared tests. In practice, algorithmic efficiency and computing power are essential for testing existing ocean models by such 'inverse methods' (Chua and Bennett, 2001; Bennett, 2002). The advancement of each of these three technologies (basin scale arrays, mathematical method, and high performance computing) enables the testing of ocean circulation models in the same way as any other scientific hypothesis. Within this framework, an 'ocean model' now includes not only equations of motion, initial values and boundary conditions, but also hypotheses about the errors in all these assumptions. Ocean models have always been attended by an error hypothesis, if only that all errors are zero. We shall enumerate these hypotheses below. The formal evaluation of models is in its infancy in physical oceanography but is the foundation of all experimental science. The situation is, in some respects, easier to grasp when models are used to predict the occurrence of a particular event (for example, an elementary particle of a particular energy and other specific characteristics). It is so unfamiliar in oceanography that we find it useful to reproduce the following quote from Stommel (1954).

*"By far the greatest part of physical oceanographic knowledge has been accumulated in the following way:*

*(1) a grand cruise, or expedition, brings back many hydrographic stations' worth of data;*

*(2) extensive plots, graphs, and tabulations of the data are made and published for the benefit of future generations;*

*(3) certain of the more striking features of the data plots are noted;*

*(4) some plausible hypotheses are advanced to explain them.*
*This procedure usually exhausted the energy of those involved, and almost always the funds, and the study usually stopped at this stage…*
*All the above steps are absolutely necessary, of course, otherwise we would know nothing at all about the ocean as it really is. But for the full development of the science there must be one additional step:*

*(5) The plausible hypotheses must be tested by specifically designed observations. In this way theories can be rejected or accepted, or may be modified to become acceptable."*

We are pleased to be able, at last, to heed Stommel's directives, and thereby to bring physical oceanography a step closer in approach to its parent sciences.

In previous investigations (Bennett *et al.*, 1998, 2000; Ngodock *et al.*, 2000) we have tested two somewhat simplified tropical models. The first was a coupled atmosphere-ocean anomaly model after Zebiak and Cane (1987), with a $1\frac{1}{2}$ layer reduced-gravity linear atmosphere over a $2\frac{1}{2}$ layer reduced gravity ocean. The second was a $2\frac{1}{2}$ layer reduced-gravity, non-anomaly, Primitive-Equation ocean model after McCreary and Yu (1992).

The coupled anomaly model could not be reconciled with 12-month and 18-month segments of monthly mean wind, sea-surface temperature (SST) and depth of the 20°C isotherm

($Z20$), to within acceptable levels of error. Specifically, the data misfits or residuals were within the measurement tolerances, but the dynamical residuals were excessively large and dominated the dynamical balances. The Primitive-Equation ocean model, forced either by climatological or real-time winds, could be reconciled with SST to within about one standard error for each piece of information. However the tendency of the fully nonlinear model to break down during assimilation, owing to vanishing layer thicknesses, led us to abandon it before testing at higher vertical resolution.

More physically complete than the above models, but less so than the Primitive Equations in the form widely used by Philander and others (for example, Philander and Siegel, 1985), is the reduced–gravity model of Gent and Cane (Gent and Cane, 1989). They effect the reduced–gravity filter by assuming that there is no horizontal pressure gradient below a deep bounding isotherm. Any entrainment velocity across this isotherm is also disallowed. The reduced–gravity filter eliminates the fast, external gravity-wave mode, thereby reducing computing times typically by 50%. The reduced dynamics have been alleged to be plausibly suitable for modeling seasonal-to-interannual variability in the tropics. Longer times scales over which, for example, the influences of bathymetry and deep thermohaline circulation are repressed, are beyond the representativeness of this model system. Comprehensive descriptions of the model may be found in Gent and Cane (1989), Gent (1991) and Kaufman and Gent (1999). In order to carry out forward integrations with the model, it is necessary to prescribe initial conditions for all prognostic variables, and also values for all coefficients in the parameterizations of processes unresolved by the model. The extent to which this model and the TAO observations can be reconciled, in a weighted least–squares sense, is the subject of our effort here. We emphasize that the reconciliation need only be within the hypothesized uncertainties in the observations (as far as the observations can be related to the model prognostic variables) *and in the model*. We shall describe below one restriction upon the inverse model that we have found essential in order to obtain solutions.

A complete description of the inverse model, optimization algorithm and software is very lengthy. The variational optimization algorithm employed here has been in development for almost two decades (Bennett and McIntosh, 1982; Bennett, 1992; Bennett and Thorburn, 1992; Egbert *et al.*, 1994). A detailed account for a global Numerical Weather Prediction model may be found in Bennett *et al.* (1996, 1997). An outline of the algorithm and its implementation may be found in Chua and Bennett (2001); Bennett (2002) is a complete text. An online interactive tutorial is available at `http://iom.asu.edu`. In the interest of brevity, the model and inversion algorithm are not described here, and just sufficient schematic mathematics is used to facilitate discussion of scientific issues. The only detailed development here is an analysis of degrees of freedom, which we have not found elsewhere.

We mention at this point that the TAO temperatures are collected at fixed depths, while the Gent–Cane model computes the temperatures of layers having depths which are fixed fractions of the depth of the bounding isotherm. Hence the measurement functionals which map model temperatures to observed temperatures are nonlinear interpolations. They compound

the nonlinearity of the inverse problem (the Gent–Cane model dynamics are nonlinear); the problem is solved iteratively.

The outline of this paper is as follows. The TAO data and the measurement functional for the Gent–Cane model are discussed in Section 2; details are relegated to an Appendix. The hypothesis for the model errors and data errors is formulated in Section 3; details of the hypothesized error covariances may be found in another Appendix. Experiments and results for the 1997–1998 El Niño (December 1997–March 1998) are presented and discussed in Section 4; the critical analyses of data residuals and model residuals are reserved for a separate section (5). These two sections emphasize residuals fields and diagnostics at the expense of the inverse fields themselves, as the latter fields conform very closely to the data. Finally, a summary and discussion are given in Section 6.

## 2. Data

Ocean temperature and currents, along with many meteorological variables, are being collected by the TAO array in the tropical Pacific. For a comprehensive view of the array and the entire TAO project, one can visit the project website:

`http://www.pmel.noaa.gov/tao/proj_over/proj_over.html`

The data employed here are monthly–mean values of temperature $T$ at the surface and at about ten depths above 500 m. The western sampling scheme is:

1, 25, 50, 75, 100, 125, 150, 200, 250, 300, 500 m;

the eastern scheme is:

1, 20, 40, 60, 80, 100, 120, 140, 180, 300, 500 m.

In addition, a few sites (e.g., along the equator) have higher vertical resolution. The thermistor depths vary from mooring region to mooring region, with more shallower sensors in the east, for example. The monthly-mean instrumental error is 0.4 K (McCarty *et al.*, 1997). We assume that measurement errors are uncorrelated, that is, the measurement error covariance matrix is diagonal with values $0.16\,\mathrm{K}^2$. In our earlier studies (Bennett *et al.*, 1998, 2002) involving the Zebiak–Cane intermediate coupled model, which has a '1.5 layer' atmosphere and a '2.5 layer' ocean, the only data we assimilated were monthly means of sea surface temperature (SST), surface winds and and the depth of the 20°C isotherm ($Z20$). It is clear that the 2000 km zonal sampling and monthly–mean temporal sampling alias the Tropical Instability Waves (e.g., Philander, 1990), which have 2 K amplitudes in temperature, 20–40 day periods and 1000 km zonal length scales. It might be argued that these aliased waves contribute to the measurement error. The Gent–Cane model includes the dynamics of shear instability, which is thought to be the mechanism of the TIWs. Also, the wind analyses used here resolve the temporal and zonal scales that would be amplified by the instability (the possible importance of narrow meridional wind structure in TIW dynamics is

just emerging from NSCAT data: Chelton *et al.*, 2000). We conclude that the model should simulate the amplitude and phase of TIWs, and any failure to do so is a consequence of error in the wind stress, in the surface boundary layer parameterizations, or in the subsurface mixing parameterizations. In particular, we conclude that the TIWs do not contribute to measurement error. The monthly-mean measurements would indeed alias the model TIWs just as they would alias real TIWs, but this is a failing of monthly-mean sampling rather than errors in an individual measurements. Daily-mean TAO data would not alias the TIWs in time. However the inverse, as weighted, could not fit data of such relatively high frequency.

High-frequency, nonhydrostatic internal waves can arise as part of a broad-band response to intensive forcing on resolved scales. The Gent–Cane model is not capable of simulating these motions at all, so we would regard their contributions to the data as measurement errors. Now, a running average over time $T_a$ applied to a sinusoidal signal of amplitude $A$ and period $\tau$ yields a signal with amplitude $a = A\tau/(2\pi T_a)$. If $A = 2\,\mathrm{K}$, $\tau = 5\,\mathrm{days}$ and $T_a = 30\,\mathrm{days}$, then $a = 0.06\,\mathrm{K}$. We conclude that such internal motions do not lead to significant measurement errors. Indeed, the time scale $\tau$ in the numerator is a gross upper bound on the period of nonhydrostatic internal waves.

The TAO data are collected at certain depths $z$, while the model fields are defined on surfaces of constant $s$, where $s$ is a fraction of the depth of the bounding isotherm. It is necessary therefore to interpolate model temperatures between $s$–surfaces in order to obtain model values at an arbitrary depth $z$. Piecewise linear interpolation between layers is functionally nonsmooth, since layer depths are dependent variables, and such functionality is inadmissible in variational assimilation. We have therefore devised and employed a global, nonlinear but functionally smooth interpolation scheme, described in detail in Appendix A. The global scheme is in fact functionally analytic, that is, infinitely differentiable.

## 3. The Gent–Cane model as a formal hypothesis

### *a. Preliminaries*

Our computational domain is (124E—85W, 29S—29N), in the upper ocean above 9°C. The spatial resolution is 1 degree zonally, 1/3 degree meridionally at the equator expanding poleward to 1 degree, and there are 21 layers in the water column above 9°C. The summed layer thicknesses are:

$$10, 20, 35, 50, 65, 80, 100, 120, 140, 160, 180, 200, 225, 250,$$
$$275, 300, 330, 360, 405, 450, 500\ \mathrm{m}.$$

The vertical resolution is uncommonly high for the Gent–Cane model. It is necessitated by the poor performance of the model at lower resolution, as became increasingly evident during preliminary integrations. To establish the model accuracy, some forward model integrations were carried out in carefully controlled circumstances with different vertical resolutions. All were initialized with the result of a 5–year, $21\frac{1}{2}$–layer spin up forced by monthly means of reanalyzed surface fluxes (described in Appendix B); the initial

conditions for the lower–resolution integrations were obtained by interpolating from the $21\frac{1}{2}$–layer initial conditions. The forward integrations were of three months' duration, covering September, 1997–November, 1997. Reanalyzed surface fluxes were again employed. The monthly–mean surface and subsurface temperature predictions were compared to the 1840 available TAO monthly–mean surface and subsurface data. For $7\frac{1}{2}$–layer, $15\frac{1}{2}$–layer and $21\frac{1}{2}$–layer integrations, the rms errors were, respectively, 5.81 K, 5.09 K and 2.84 K. Thus $21\frac{1}{2}$–layer resolution is the coarsest that makes any sense as the basis for advanced data assimilation, given that the standard errors of the monthly–mean data are 0.4 K. A clean comparison is not available for inversions having different vertical resolutions. In brief, the preliminary lower–resolution inversions did not fit the observations and, like the intermediate coupled models (Bennett *et al.*, 1998, 2000), grossly failed their significance tests. Preliminary integrations of the Gent–Cane model also made clear that uniform, constant, vertical eddy diffusivities lead to excess downward mixing of heat in particular. The simplest alternative is the KPP parameterization scheme of Large, McWilliams, and Doney (Large *et al.*, 1994). The scheme computes the mixed-layer depth as that which yields a critical value for a bulk Richardson number $Ri_b$; below the mixed-layer depth there are variable diffusivities which are simple functions of a gradient Richardson number $Ri_g$. The formula for $Ri_b$ is not smooth and so has no adjoint. The principal difficulty is the discontinuous derivative of certain universal functions of stability, at neutral stability. According to C. Paulson (personal communication, 2003), there is no experimental evidence to invalidate an arbitrary alteration of the slope of universal functions on the stable side, so as to render the functions continuously differentiable. However, such a variation of the KPP scheme would require comprehensive testing for impact. In addition, the empirical intricacies of even the regularized formula for $Ri_b$ lead to excessively complicated adjoints, and some algebraic relief is in order. This too requires comprehensive testing for impact. The inversions reported here have been carried out with an assumption of constant mixed-layer depth (10 m, identified with the uppermost model layer, in which the diffusivities are held constant), and with the standard $Ri_g$-dependent diffusivity in the 'interior' below the mixed layer. Forward integrations with the tangent linearization of the KPP-interior scheme yielded negative effective diffusivities, so alternative Picard iteration schemes were required in order to deal with this nonlinear aspect of the variational problem.

The model and variational equations have been coded in Fortran-95 for optimal performance on the CM-500e and IBM SP-4 (anonymous `ftp.oce.orst.edu, /dist/chua/IGC`).

### *b. The extended model*

The Gent–Cane model and the data are represented schematically as

$$\mathbf{D}(\mathbf{U}) = \mathbf{F} + \mathbf{f} \tag{1}$$

$$\mathbf{U}(\mathbf{x}, s, 0) = \mathbf{U}_I(\mathbf{x}, s) + \mathbf{i}(\mathbf{x}, s) \tag{2}$$

$$\mathbf{d} = \boldsymbol{\mathcal{M}}[\mathbf{U}] + \boldsymbol{\epsilon}. \tag{3}$$

where $\mathbf{x}$ is the Eulerian horizontal coordinate and $s$ the Lagrangian or thermodynamically scaled vertical coordinate, $\mathbf{U}$ is the multivariate ocean state ($u, v, w, T, \ldots$, etc), $\mathbf{D}$ is the vector-valued nonlinear differential operator that expresses the dynamics of the Gent–Cane model, and $\mathbf{F} = \mathbf{F}(\mathbf{x}, s, t)$ is the first guess forcing field including all distributed and superficial forcing such as subsurface radiative heating, surface wind stresses, etc. To continue, $\mathbf{f} = \mathbf{f}(\mathbf{x}, s, t)$ denotes the error field in the equations of motion, $\mathbf{i}$ denotes the error field in the first-guess initial values $\mathbf{U}_I$, and $\boldsymbol{\epsilon}$ the error in the data $\mathbf{d}$. One component of $\mathbf{d}$ is, for example, the monthly–mean temperature at a depth of 100 m on the mooring at (155W, 8S). Thus, the TAO array in mimicked mathematically by the action of the functional $\boldsymbol{\mathcal{M}}$ that maps $\mathbf{U} = \mathbf{U}(\mathbf{x}, s, t)$, the mathematical representation of the ocean state, into a vector of real numbers, one per datum: $\mathbf{U} \to \boldsymbol{\mathcal{M}}[\mathbf{U}] \in \mathbb{R}^M$. Note that the vector–valued measurement functional $\boldsymbol{\mathcal{M}}$ is nonlinear: see (15)–(17) in Appendix A. The error $\mathbf{f}$ in the equations may owe, in this formulation, either to errors in the dynamics or in the first-guess forcing field $\mathbf{F}$. The error $\boldsymbol{\epsilon}$ owes either to instrumental error including engineering considerations such as mooring motion, and to error of unrepresentativeness (the reduced–gravity Gent–Cane model cannot simulate barotropic Rossby waves, for example).

Let us now assume that the errors $\mathbf{f}$, $\mathbf{i}$ and $\boldsymbol{\epsilon}$ are random, having first and second moments prescribed by the null hypothesis $\mathcal{H}_0$:

$$\mathcal{H}_0 \begin{cases} E\{\mathbf{f}(\mathbf{x}, s, t)\} = E\{\mathbf{i}(\mathbf{x}, s)\} = E\{\boldsymbol{\epsilon}\} = \mathbf{0} & \\ E\{\mathbf{f}(\mathbf{x}, s, t)\mathbf{f}^T(\mathbf{x}', s', t')\} & = \mathbf{C}_{ff}(\mathbf{x}, s, t; \mathbf{x}', s', t') \\ E\{\mathbf{i}(\mathbf{x}, s)\mathbf{i}^T(\mathbf{x}', s')\} & = \mathbf{C}_{ii}(\mathbf{x}, s; \mathbf{x}', s') \\ E\{\boldsymbol{\epsilon}\boldsymbol{\epsilon}^T\} & = \mathbf{C}_{\epsilon\epsilon} \\ E\{\mathbf{f}\mathbf{i}^T\} = \mathbf{0}, \quad E\{\mathbf{f}\boldsymbol{\epsilon}^T\} = \mathbf{0}, \quad E\{B\mathbf{i}\boldsymbol{\epsilon}^T\} = \mathbf{0}, & \end{cases} \tag{4}$$

where $E\{\ \}$ denotes the ensemble average, and superscript $T$ the transposed vector. We hypothesize, without loss of generality, that the first moments vanish; otherwise they could be included in $\mathbf{F}$, $\mathbf{U}_I$ and $\mathbf{d}$. The autocovariances $\mathbf{C}_{ff}$, $\mathbf{C}_{ii}$, and $\mathbf{C}_{\epsilon\epsilon}$ may be provided in functional form or tabular form. As usual, the cross covariances $\mathbf{C}_{\mathbf{fi}}$, etc. are assumed, out of ignorance, to vanish (but see Bogden, 2001; Muccino and Bennett, 2004).

Functional forms and parameter values for the several covariances appearing in (4) are given in Appendix B. The time-dependent fields are assumed to be statistically stationary. The fields are all assumed to be statistically homogeneous zonally, but inhomogeneous meridionally and vertically. The subsurface fields are all assumed uncorrelated in the vertical. As in our earlier investigations we adopt, out of ignorance, the simplest 'bell–shaped' choices for the functional forms. We assume 100% error in the initial analyses. We assume that the errors in the dynamical equations are dominated by the parameterization of vertical mixing fluxes, and we assume that the errors in the KPP-parameterized flux divergences

are 100% of the parameterized flux divergences themselves (even greater, for the eddy heat flux of heat). The remaining choices for variances, and for decorrelation scales, are based on our analysis of TAO climatology (see Appendix B); other climatologists may well make other choices. However the essential features of our detailed hypothesis are simple and robust: significant levels of error are assumed in the dynamical and initial constraints, and the decorrelation scales imply that there are a large number of effective degrees of freedom in the errors or constraint residuals (see Section 5). Thus the extended model should have considerable flexibility to fit the high quality TAO data.

Our detailed hypothesis is indeed highly detailed. Once it is conceded that a complex ocean model is dynamically imperfect, and that the imperfections have a range of variability, quantifying that variability involves a great deal of as yet poorly known information about the ocean. No doubt many of our assumptions are naïve, but the conventional assumption of a perfect model is more naïve. The conventional assumption is not really less detailed: the many error variances are all assumed to vanish.

Armed with our hypothesis, we estimate the ocean state $\mathbf{U}$ as the extremum $\hat{\mathbf{U}}$ of the maximum–likelihood estimator $\mathcal{J}$ for the multivariate Gaussian random fields $\mathbf{f}$, $\mathbf{i}$ and $\boldsymbol{\epsilon}$. The estimator or penalty functional $\mathcal{J}$ is quadratic in $\mathbf{f}$, $\mathbf{i}$, and $\boldsymbol{\epsilon}$ but is nonlinear in $\mathbf{U}$. Again, $\mathbf{U}$ is related to these fields through (1)–(3). The estimate $\hat{\mathbf{U}}$ satisfies the Euler–Lagrange equations for extrema of $\mathcal{J}$. In less formal terms, our estimate of the ocean state is a weighted least–squares best fit to the model and the data. The weights are reciprocals, in an integral–equation sense, of the hypothesized covariances (4). See Chua and Bennett (2001) or Bennett (2002) for details.

The results presented in Section 4 will include, in particular, both the first–guess (prior) penalty $\mathcal{J}_F \equiv \mathcal{J}[\mathbf{U}_F]$ (where the first–guess solution $\mathbf{U}_F$ satisfies the forward model $\mathbf{D}(\mathbf{U}) = \mathbf{F}$ subject to $\mathbf{U}(\mathbf{x}, s, 0) = \mathbf{U}_I(\mathbf{x}, s)$), and also the inverse or posterior penalty $\hat{\mathcal{J}} \equiv \mathcal{J}[\hat{\mathbf{U}}]$. Note that $\mathcal{J}_F$ consists of weighted data misfit only, while $\mathcal{J}[\hat{\mathbf{U}}]$ contains weighted misfits to the initial conditions and to the dynamics as well as misfits to the data.

## 4. Experiments and results

### *a. Three-month nonlinear inversions*

The inverse estimate $\hat{\mathbf{U}}$ for the ocean state is found as a solution of the Euler–Lagrange equations for extrema of the penalty functional $\mathcal{J}[\mathbf{U}]$. The equations are nonlinear, owing to the nonlinearity of the dynamical model itself, and of the measurement functional that relates model layer temperatures to temperatures at depths. The Euler–Lagrange equations are solved in several stages, the first of which is a Picard or functional iteration that generates a sequence of linear Euler–Lagrange problems. Each of these problems is solved in turn by an indirect or iterative application of the representer algorithm (Egbert *et al*., 1994; Amodei, 1995). If the sequence of solutions converges, the limit solves the nonlinear Euler–Lagrange problem.

Convergence is delicate. The conventional Picard iteration is the tangent linear scheme (Lacarra and Talagrand, 1988), that tends to yield a negative effective eddy viscosity for the KPP interior parameterization scheme in the tropics. The KPP interior scheme is instead subjected here to an alternative Picard iteration, our 'Scheme A' (Bennett and Thorburn, 1992; Chua and Bennett, 2001; Bennett, 2002), that necessarily yields positive diffusivities. To illustrate the two schemes, consider two choices for linearizing iterations on the product $ab$: the tangent linearization is $a_n b_{n-1} + a_{n-1}(b_n - b_{n-1})$; Scheme A is simply $a_{n-1}b_n$. It has also been necessary, in the interests of convergence, to impose the continuity equations and initial conditions for layer thickness as *strong constraints*; that is, no distributed volume sources or sinks, nor initial volume errors, are allowed as controls. Without such a restriction on its volumetrics and initial volume values, the deep bounding isotherm tends to outcrop. These contraints could be relaxed if there were a sufficiency of regularly spaced but unbinned and uniformly deep temperature data that could enable the construction of proxy data for the depth of the bounding isotherm. Such data would inhibit any unrealistic outcropping. In the further interest of convergence and computational efficiency, inversion is restricted to three–month intervals during the major El Niño event of December 1996–March 1998 (McPhaden, 1999a, b). Finally, convergence of the Picard iteration is accelerated by the inclusion of a relaxation effect in the forward model. The effect vanishes from the forward model in the limit, but a small 'ghost' remains in the adjoint model in the limit. Thus the reported inversion is very slightly suboptimal; details may be found in Appendix C.

A great many three–month inversions were performed with varieties of parameters. We present here the one inversion that shows the Gent–Cane model in by far the best light, to the extent that we are able to construct fields that fit the TAO data to within experimental error, and that fit the equations of motion with small residuals at each point and time. This experiment is arguably a successful reanalysis of the TAO data in the smoothing interval September–October–November of 1997 ('9/97–11/97'). As discussed above, all constraints except those for layer thickness are weak, so this inversion is denoted 'Exp. W.' Its foil, a pure strong–constraint inversion for the same time interval, is denoted Exp. S and is also discussed here.

Shown in Figure 1 are the common logarithms of the first guess penalty values $\mathcal{J}_F$ and inverse penalty values $\hat{\mathcal{J}}$ in each iterate, for seven Picard iterates in Exp. W. These are the penalties respectively for the first guess or prior $\mathbf{U}_F$ and for the inverse or posterior $\hat{\mathbf{U}}$. The former penalty consists of data misfit alone, while the latter contains dynamical, initial and data misfits. Each iterate involves the solution of a linear Euler–Lagrange problem. Note that the first guess forcing and initial condition in each iterate are respectively the priors $\mathbf{F}$ and $\mathbf{I}$, rather than the posteriors $\mathbf{F} + \hat{\mathbf{f}}_{n-1}$, $\mathbf{U}_I + \hat{\mathbf{i}}_{n-1}$ from the preceding iterate[5]. The convergence is almost entirely monotone, but need not be: these iterates are not steps in a gradient search; rather, they are steps in a Picard iteration on the nonlinear Euler–Lagrange

5. It may be proved that, were the latter choices made for the forcing and initial fields at each iterate, then the sequence of inverse solutions $\hat{\mathbf{U}}_n$ would converge to a perfect fit to the data, regardless of the data weighting.

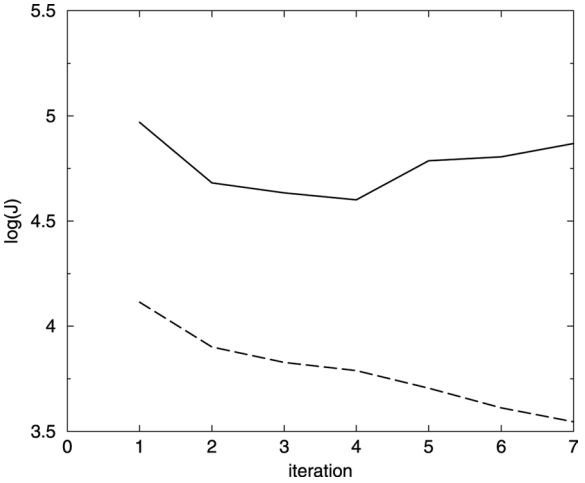


Figure 1. Common logarithms of first–guess penalty $\mathcal{J}_F$ (solid line) and inverse penalty $\hat{\mathcal{J}}$ (dashed line) for 7 Picard iterations on the nonlinear Euler-Lagrange equations, Exp. W. Each iterate is a linear Euler-Lagrange problem.

problem. No sign of solution breakdown, such as isolated outcropping of the deep bounding isotherm, has appeared by the seventh iterate.

Equatorial sections of monthly-mean temperature for the third month of Exp. W (November 1997) are shown in Figure 2. Panel (a) is the conventional integration of the nonlinear Gent–Cane model plus KPP interior scheme, panel (b) is the NOAA PMEL standard bicubic spline interpolation of the TAO data (Soreide *et al.*, 1996) and panel (c) is the nonlinear inverse solution (seventh Picard iterate on the nonlinear Euler–Lagrange equations). The first guess (a) is everywhere too warm, while the inverse (c) shows little significant nonlocal error. The small scales in the inverse (c) are probably not credible. The excess warmth of the first guess shown in (a) is not visually striking, as it is 'only' a matter of about 2–3 degrees K. On the other hand, warming a 500 m column of water by 2.5 K in three months requires the very considerable surface heat flux of 0.5 kW $m^{-2}$. The penalties are far more striking indicators of model performance: the standard error of measurement is 0.4 K and so the weighted and squared data misfit for the first guess (a) is about 40 per datum.

The model is, again, driven by reanalyzed NCEP surface fluxes and monthly–mean FSU winds. If these were correct, and the model were correct in every other respect as well, then the true state of the ocean *would* be recovered, even though the real atmosphere is in a dynamic balance with the real ocean and even though the exchange of heat, in particular, almost certainly does depend upon the ocean temperature. What is suspect here is the response of the model to the inevitable error in the best available analysis of, say, just the imposed surface fluxes of heat: the response would be affected by a temperature–dependent air–sea exchange. We could have introduced a no–doubt flawed parameterization of such a

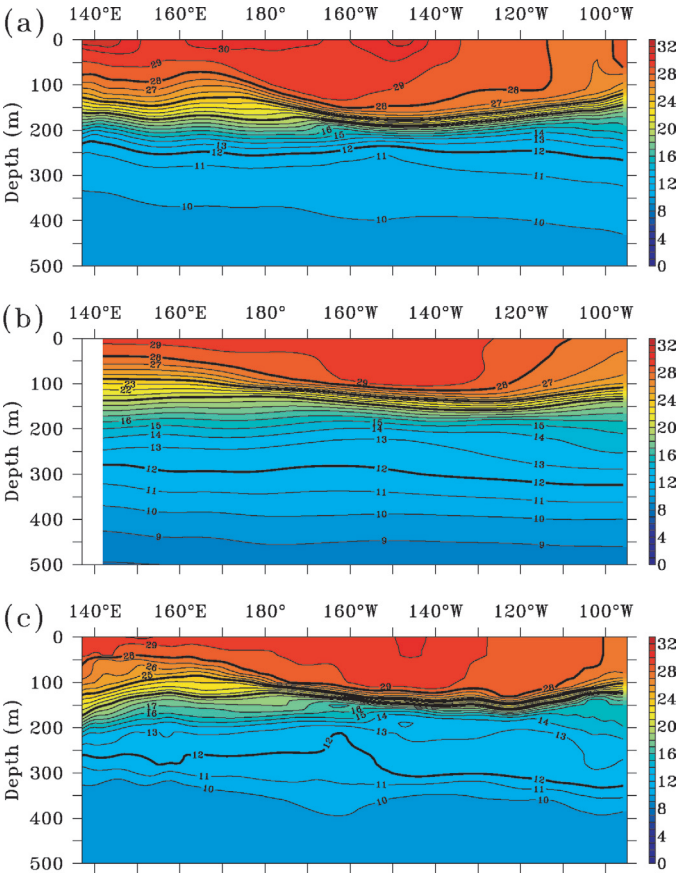


Figure 2. Equatorial temperature sections of monthly mean temperature (November 1997) in degrees°C: (a) conventional integration of the Gent–Cane model plus KPP interior scheme; (b) NOAA PMEL standard bicubic spline interpolation of monthly mean TAO data (Soriede *et al.*, 1996); (c) monthly mean of the nonlinear inverse solution (Exp. W) combining the hourly–stepped model and the monthly mean data. Contour interval: 1.0 C.

process. However, it is not clear that imposing the inevitably–erroneous reanalyzed fluxes through a crude feedback loop would lead to a more realistic solution. Yet it is generally the case, in the equatorial Pacific on ENSO time scales, that surface fluxes damp SST anomalies generated by ocean dynamical processes. So, if the feedback loop were at all realistic, the impact of flux errors would be damped. The impact of the errors could only be truly resolved by knowing the true fluxes. In the absence of such knowledge, we treat the reanalyzed surface fluxes as weak constraints, and we hypothesize surface flux errors having the same variance as the reanalyzed fluxes themselves ('100% error'). The residual in the surface heat flux is a maximum–likelihood assessment of the flux error, in light of the TAO data, via the Gent–Cane model.

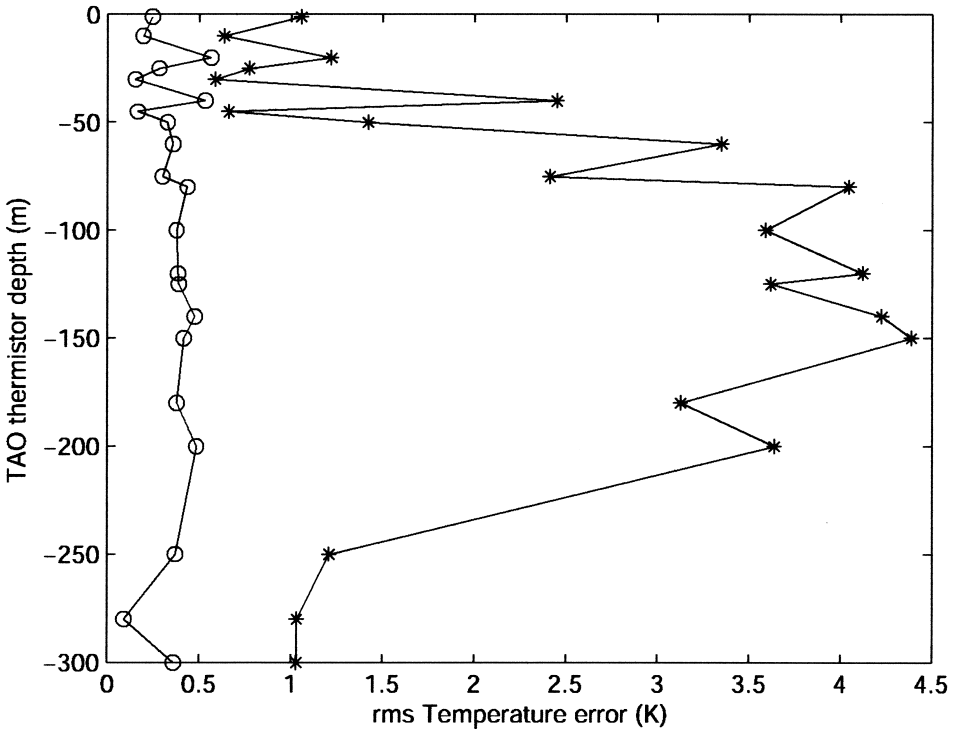


Figure 3. Arithmetic means of the absolute values of the misfits to monthly–mean temperature TAO data at TAO depths, for all TAO moorings and for September, October, November 1997. Asterisks: first–guess or prior misfit. Circles: inverse or posterior misfit. The number of data at each depth is given in Table 1.

An analysis of a least–squares inversion should properly commence with the first–guess (prior) and inverse (posterior) penalties. However, we commence instead with a more intuitive statistic. The mean magnitudes of the misfits between the monthly–mean TAO temperature at each TAO depth, and the first guess and inverse solutions, are plotted in Figure 3. The mean is taken for all TAO moorings in September, October and November 1997. The number of monthly–mean temperature data at each depth, for all moorings and the three months, vary widely with depth: see Table 1. This variability in sample size is responsible for much of the roughness seen in Figure 3. However, the essential features are clear. By far the largest first–guess misfits are found between 75 m and 200 m, well below the surface mixed layer throughout the equatorial Pacific. The magnitude of the misfit is as high as 4.4 K, at 150 m. This may be compared with the measurement error of 0.4 K. In comparison, the inverse misfits are all less than 0.6 K. It is evident that the $21\frac{1}{2}$–layer forward model is underperforming principally near 150 m. That is, its faults owe principally to the subsurface dynamics, and far less to either the reanalyzed surface fluxes or the assumption of a constant mixed–layer depth.

Table 1. Number of TAO monthly–mean temperature data at TAO depths, for all TAO moorings and September, October, November, 1997.

| Depth (m) | Number |
|---|---|
| 1 | 182 |
| 10 | 9 |
| 20 | 68 |
| 25 | 110 |
| 30 | 3 |
| 40 | 66 |
| 45 | 6 |
| 50 | 107 |
| 60 | 79 |
| 75 | 107 |
| 80 | 79 |
| 100 | 183 |
| 120 | 79 |
| 125 | 107 |
| 140 | 78 |
| 150 | 107 |
| 180 | 67 |
| 200 | 113 |
| 250 | 106 |
| 280 | 3 |
| 300 | 181 |

Shown in Table 2 are the prior values $\mathcal{J}_F$, and posterior or inverse values $\hat{\mathcal{J}}$, of the penalty functionals for Exp. W. The inverse penalty $\hat{\mathcal{J}}$ is partitioned into two additive parts: $\hat{\mathcal{J}}_{model}$ and $\hat{\mathcal{J}}_{data}$. The former includes initial penalties as well as dynamical penalties. Consider the first guess penalty $\mathcal{J}_F$. The first–guess solution $\mathbf{U}_F$ exactly satisfies the forward model linearized about the preceding inverse estimate (here, the third), with first–guess initial value $\mathbf{U}_I$, and with first–guess forcing $\mathbf{F}$. Thus $\mathcal{J}_F$ is the weighted squared difference between the 'measured' first–guess solution and the data. The measurement functional $\boldsymbol{\mathcal{M}}$ is also linearized about the preceding inverse. The weight in $\mathcal{J}_F$ is the matrix inverse of the measurement error covariance matrix; both matrices are diagonal here. If this

Table 2. First–guess ($\mathcal{J}_F$) and inverse ($\hat{\mathcal{J}}$, $\hat{\mathcal{J}}_{model}$, $\hat{\mathcal{J}}_{data}$) penalties for three-month inversions (Exp. W and Exp. S); note that $\hat{\mathcal{J}} = \hat{\mathcal{J}}_{model} + \hat{\mathcal{J}}_{data}$. The number of data $M$ is also $E(\hat{\mathcal{J}})$, the expected value of the total inverse penalty.

| | Exp. W | Exp. S |
|---|---|---|
| | 9/97–11/97 | 9/97–11/97 |
| $M$ | 1840 | 1840 |
| $\mathcal{J}_F$ | 73750 | 73750 |
| $\hat{\mathcal{J}}$ | 3510 | 7438 |
| $\hat{\mathcal{J}}_{model}$ | 1821 | 3122 |
| $\hat{\mathcal{J}}_{data}$ | 1689 | 4315 |

solution were 'good,' then $\mathcal{J}_F$ would be about equal to the number of data $M$, here 1840, since each datum would differ from the corresponding value of the prior solution by about one standard error ($\sigma_T = 0.4$ K). In fact the difference between the first–guess solution (Exp. W) and the data is about $\sqrt{73750/1840} = 6.3$ standard errors of temperature measurement, or about 2.5 K. The inverse data penalty is $\hat{\mathcal{J}}_{data} = 1689$; the implied rms data misfit ($0.4\sqrt{1689/1840} = 0.38$ K) is less than the hypothesized measurement error for the monthly-mean TAO temperature data ($\sigma_T = 0.4$ K). If the null hypothesis $\mathcal{H}_0$ were correct, then the inverse penalty $\hat{\mathcal{J}}$ (inverse model penalty plus inverse data penalty) would be the chi-squared variable with $M$ degrees of freedom (e.g., Bennett, 1992). Thus its expected value is $M = 1840$, and its standard deviation is $\sqrt{2M} = 61$. In fact, $\hat{\mathcal{J}} = 3510$. That is, $\hat{\mathcal{J}}$ differs from its expected value by 27 standard deviations. There is only a microscopically small probability that the null hypothesis $\mathcal{H}_0$ is correct, and that this result is 'bad luck.' This is a disconcerting result, as the hypothesis allows very generous levels of error in the dynamics in particular. It also allows many degrees of freedom in the dynamical errors (see Section 5), with which the data may be fit.

Next, consider the means and variances of the various penalty values discussed so far for Exp. W. Again, the expected or mean value of $\hat{\mathcal{J}}$ is always $M$, the number of data. The means of the penalty values $\mathcal{J}_F$, $\hat{\mathcal{J}}_{model}$ and $\hat{\mathcal{J}}_{data}$, and the variances of all these penalty values, depend upon the so-called representer matrix which is the key to each linear inversion (Bennett *et al.*, 2000; Bennett, 2002). Explicit, direct computation of this $M \times M$ matrix is prohibitive, requiring $M$ adjoint and $M$ forward model integrations; the advantage of the indirect inversion algorithm employed here is that it enables computation of the inverse without explicitly constructing the representer matrix (Egbert *et al.*, 1994). However, the matrix may be approximated by Monte Carlo methods, which are just sufficiently accurate for the purpose of approximating the means and variances of penalty values. Statistical simulation is possible, since the representer matrix is also a covariance matrix (Bennett, 1992; 2002). Random forcing errors $\mathbf{f}$ and random initial errors $\mathbf{i}$ are synthesized so that they have the covariances in the null hypothesis (4). The synthesis details are tedious but standard signal processing, (see Bennett, 2002). These synthetic random inputs lead, by forward integration, to sample estimates of the error in the first guess solution $\mathbf{U}_F$. The sample covariance of the errors in the $M$ 'measurements' of $\mathbf{U}_F$ is an approximation to the representer matrix. The issue of sample size is important, but is less critical for crude diagnostics than for an accurate state estimate. The penalty values are gross statistics of the inversion and so their sample estimates stabilize rapidly: see Table 3. The smoothing interval is 9/97–11/97 (Exp. W); the forward model, the adjoint models and the measurement functionals are linearized about the third Picard iteration. Sample estimates of one column of the representer matrix itself (not shown) have not converged, even after 500 samples, to the column computed from the Euler–Lagrange equations. The sample estimate of one diagonal entry of the representer matrix is also shown in Table 3. Note that the entire representer matrix could be calculated from the Euler–Lagrange equations, with $M = 1840$ forward and $M = 1840$ backward integrations. But, again, sample estimation suffices for moments of $\mathcal{J}_F$, etc.

Table 3. Expectation values and standard deviations of first–guess and inverse penalties, for Exp. W. Recall $E(\hat{\mathcal{J}}) = M$. These values depend upon the first–guess data misfit **h** and the representer matrix or 'measured' background error covariance **R**, and are obtained as Monte Carlo estimates based on 194, 385, and 502 samples. Only the forward model is required (tangent linearization around the sixth Picard iterate). For comparison, one element of **R** is computed deterministically by solving the Euler-Lagrange equations.

| | (194) | (385) | (502) |
|---|---|---|---|
| $E(\mathcal{J}_F)$ | 19978 | 19841 | 19967 |
| $E(\hat{\mathcal{J}}_{model})$ | 183 | 318 | 375 |
| $E(\hat{\mathcal{J}}_{data})$ | 1657 | 1521 | 1465 |
| $\sqrt{var(\mathcal{J}_F)}$ | 4141 | 3815 | 3767 |
| $\sqrt{var(\hat{\mathcal{J}}_{model})}$ | 19 | 23 | 25 |
| $\sqrt{var(\hat{\mathcal{J}}_{data})}$ | 35 | 67 | 80 |
| $R_{3,3} = 0.7669$ | 0.9082 | 0.8972 | 0.8754 |

Comparing Tables 2 and Table 3, it is clear that every penalty value in Exp. W significantly exceeds its expected value. In particular, the inverse data penalty exceeds its expected value ($E\{\hat{\mathcal{J}}_{data}\} = 1465$) by nearly three standard deviations ($\sqrt{var\{\hat{\mathcal{J}}_{data}\}} = 80$). Moreover, $\hat{\mathcal{J}}_{model}$ (=1821) exceeds its expected value ($E\{\hat{\mathcal{J}}_{model}\} = 375$) by 58 standard deviations ($\sqrt{var\{\hat{\mathcal{J}}_{model}\}} = 25$). The null hypothesis is significantly rejected by Exp. W. Either the hypothesized measurement errors or the hypothesized model errors (dynamical or initial) are underestimates, or they all are.

*b. Alternative hypotheses*

(i) The reduced penalty $\hat{\mathcal{J}}$ for preliminary Exp. W is 3510, while the number of data $M$ is 1840. If all the first-guess standard errors were rescaled by $\sqrt{3510/1840} = 1.38$, then the reduced penalty would be equal to its expected value and the rescaled hypothesis would seem to survive the significance test. Indeed, our knowledge of dynamical error statistics is especially vague, and such rescaling would not be unreasonable. However, while we do not have a sample set of cleanly comparable experiments, our experience with variety of experiments for this three–month interval and others during the 1997–1998 El Niño clearly suggests that the sample standard deviation of the rescaled reduced penalties for this and other intervals would greatly exceed even the rescaled expected standard deviation $\sqrt{2M} = 61$, and so the rescaled hypothesis would still be rejected. In any event, the original hypothesis is that the initial errors and subsurface flux parameterization errors are 100%, so it would serve little scientific purpose to assume them to be even larger (138%); at this point the dynamical constraints in the inversion are becoming slack. A further consideration for rescaling is that the variability amongst smoothing intervals within a single ENSO episode may be conceived as nonstationarity, rather than variability within one population. In any event, that variability contradicts the already loose error hypothesis adopted here.

(ii) Much of the recently published work on variational ocean data assimilation has allowed residuals in the initial conditions and surface fluxes only. No residuals have been allowed in any equation of motion. That is, all dynamical constraints have been 'strong.' As in our previous work, we impose the momentum and heat equations as weak constraints. The layer–thickness equations are imposed as strong constraints, otherwise we encounter divergence of the iterations on the nonlinear Euler–Lagrange equations for the best fit. A completely 'strong constraint' inversion is feasible with the algorithm used here, simply by setting all the prior dynamical error variances to zero, except for the momentum and heat equations in the uppermost layer. The latter equations must be weak constraints, as the surface fluxes only appear within these equations. For comparison, Exp. S is a repetition of the 'weak constraint' Exp. W, with just such a modification. The results for both are shown in Table 2. First, the reduced value of the total penalty $\hat{\mathcal{J}}$ for Exp. S is more than double the value for Exp. W. Second, the inverse model penalty $\hat{\mathcal{J}}_{model}$ is almost doubled, even though the dynamics in Exp. S are strong in all but the surface layer. The increase owes to the significantly greater inverse initial penalty $\hat{\mathcal{J}}_{init}$: 2582 for Exp. S, 731 for Exp. W. The inverse dynamical penalties $\hat{\mathcal{J}}_{dyn}$, summed over all layers, are 548 and 1134 respectively. Disagreement with Table 2 owes to integration error. On the other hand, the inverse dynamical penalties in the surface layer alone are 548 (recall that only the surface layer is weak in Exp. S) and 72.7, respectively. The reduced data penalties: 4316 and 1689 respectively, are equivalent to rms errors of 0.6 K and 0.38 K respectively. Broken down into monthly rms values for 9/97–11/97, these are (0.61, 0.64, 0.59) K and (0.38, 0.47, 0.31) K respectively. The increasing effectiveness of the deep dynamical controls or residuals, as time progresses, is evident. In summary, the strong constraint inversion uses excessive deep initial temperatures, and excessive surface stresses for three months, to control the deep temperatures for three months. The weak constraint inversion achieves better fit to the data with moderate initial and surface residuals, combined with moderate heat–equation residuals at depth.

Other alternative hypotheses, for the surface flux errors, are described in Appendix D.

## 5. Residuals

Conventional numerical models of stratified ocean circulation produce great volumes of output, but the volume produced by inverse models is overwhelming. In the first place, four–dimensionality is of the essence in fixed–interval smoothing. Second, there is another entire state variable: the adjoint variable. In addition, there are the penalty values as described in Section 4 but, being integrated statistics, these are of much lower dimensionality. In this largely expository development of a stratified inverse model, we have selected for emphasis the residuals from amongst the many inverse products. The residuals are obtained as adjoints convolved with the prior covariances (see e.g. Bennett, 2002)

Both the penalty $\mathcal{J}_F$ for the first–guess solution and the penalty $\hat{\mathcal{J}}$ for the inverse estimate are weighted sums of dynamical, initial and data residuals. The residuals for the refined experiment (Exp. W, Picard iteration 7) will now be analyzed in detail. All the residuals will

be seen to be smaller than the hypotheses for their standard deviations. This is seemingly in conflict with the unexpectedly large values of the penalties; the paradox is resolved by considering the effective degrees of freedom in the fit.

*a. Data residuals*

Histograms of the first–guess data residual $\mathbf{h} = \mathbf{d} - \boldsymbol{\mathcal{M}}[\mathbf{U}_F]$ and inverse data residual $\mathbf{a} = \mathbf{d} - \boldsymbol{\mathcal{M}}[\hat{\mathbf{U}}]$ are shown in Figures 4a, 4b respectively. The first guess means and standard deviations are $\mu = -1.52\,\mathrm{K}$, $\sigma = 2.03\,\mathrm{K}$, for the the inverse they are $\mu = -1 \times 10^{-2}\,\mathrm{K}$,

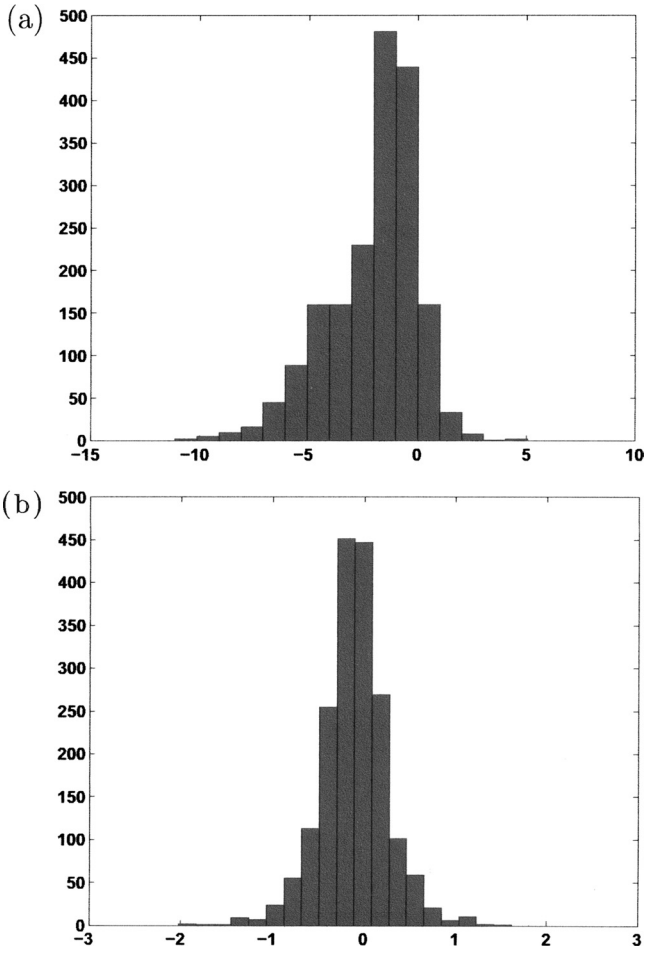


Figure 4. Histogram of (a) prior data residual $h_m = d_m - \mathcal{M}_m[\mathbf{U}_F] : \mu = -1.52\,\mathrm{K}$, $\sigma = 2.03\,\mathrm{K}$. (b) posterior data residual $a_m = d_m - \mathcal{M}_m[\hat{\mathbf{U}}] : \mu = -1 \times 10^{-2}\,\mathrm{K}$, $\sigma = 0.38\,\mathrm{K}$ ($1 \le m \le M = 1840$, Exp. W). Note the different ranges for both abscissae, which are in units of K.

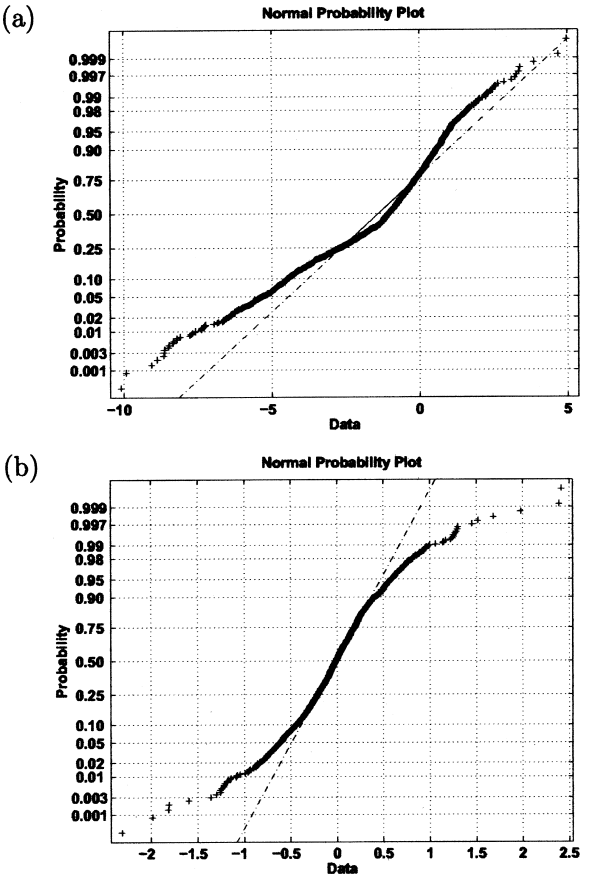


Figure 5. Normal probability plot for (a) first–guess data residual $h_m$; (b) inverse data residual $a_m$. ($1 \leq m \leq M = 1840$, Exp. W). Note the different ranges for both abscissae, which are in units of K.

$\sigma = 0.38$ K. The first–guess solution $\mathbf{U}_F$ is too warm, owing most likely to excess downward mixing of heat. The inverse $\hat{\mathbf{U}}$ is corrected by distributed heat sinks which are the inverse estimates of these mixing errors. The histograms, especially the posterior, are normal in appearance. Normal probability plots of $\mathbf{h}$ and $\mathbf{a}$ are shown in Figure 5, confirming the impression of normality, especially for $\mathbf{a}$, and also suggesting that least squares is close to being the estimator of maximum likelihood.

Nevertheless, the inverse residuals are unexpectedly too large. Their arithmetic mean is small, but their sample standard deviation is too large. Indeed, the expected value of each residual $a_m$ is zero while the expected standard error $\sigma_a^m$ is a known formula (Bennett, 2002, Eq. 2.3.24). These formulae depend upon the representer matrix $\mathbf{R}$ which, being a covariance, we approximate with Monte Carlo estimates. The estimates for $R_{3,3}$ have not converged after 502 samples (see Table 3). The correct value ($R_{3,3} = 0.7669$) is obtained by

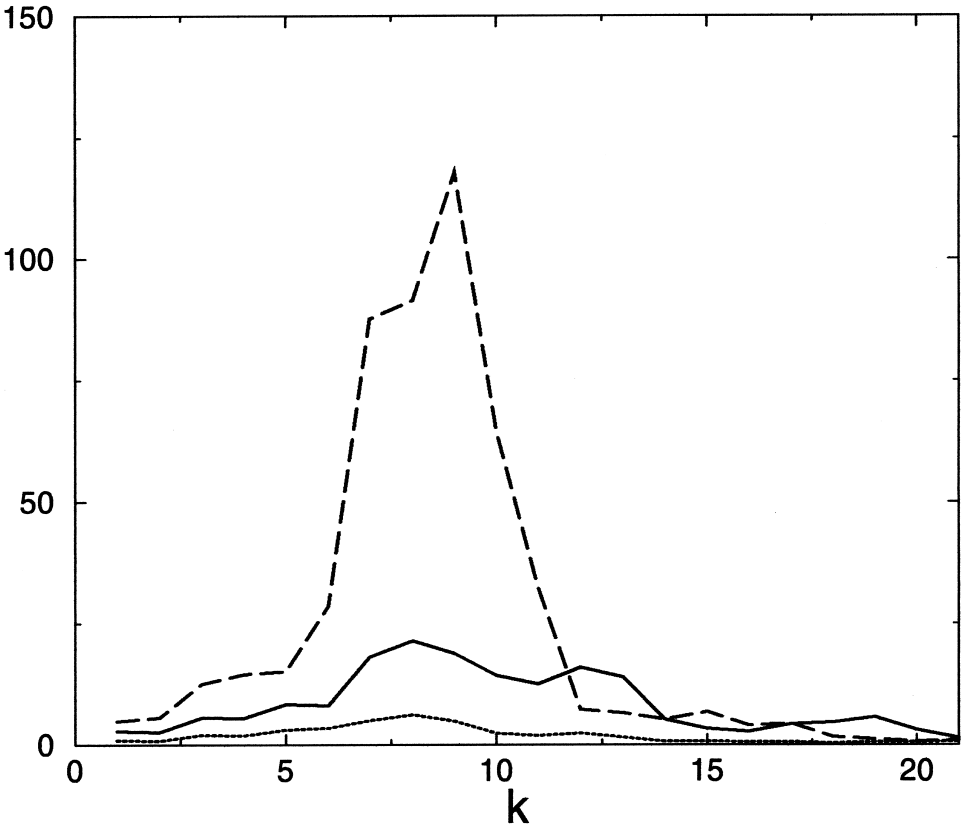


Figure 6. Vertical profiles of inverse initial penalty $\hat{\mathcal{J}}_{init}$, totalled over the horizontal, versus layer index. Solid line: zonal velocity. Dotted line: meridional velocity. Dashed line: temperature.

explicit calculation of the representer for the third component of the measurement functional $\mathcal{M}$. Such 12% inaccuracy precludes the use of Monte–Carlo methods for the computation of the inverse circulation estimate $\hat{\mathbf{U}}$ (Bennett, 2002), but suffices for "off–line" approximations of moments of inverse residuals. Defining $a'_m = a_m/\sigma_a^m$, the arithmetic mean of $a'_m$ is $-3.17 \times 10^{-2}$ while the sample standard deviation over $M$ is $\sigma'_a = 1.10$, which indicates again the poor data fit. See also Table 2, Exp. W, and Table 3: $\hat{\mathcal{J}}_{data} = 1689$, $E\{\hat{\mathcal{J}}_{data}\} = 1465$, $\sqrt{var\{\hat{\mathcal{J}}_{data}\}} = 80$.

*b. Initial residuals*

The first–guess initial penalty is exactly zero, since $\mathbf{U}_F(\mathbf{x}, s, 0) = \mathbf{U}_I(\mathbf{x}, s)$. The posterior initial penalties in Exp. W for zonal velocity (solid line), meridional velocity (dotted line) and temperature (long-dashed line) are shown in Figure 6, layer by layer, integrated over

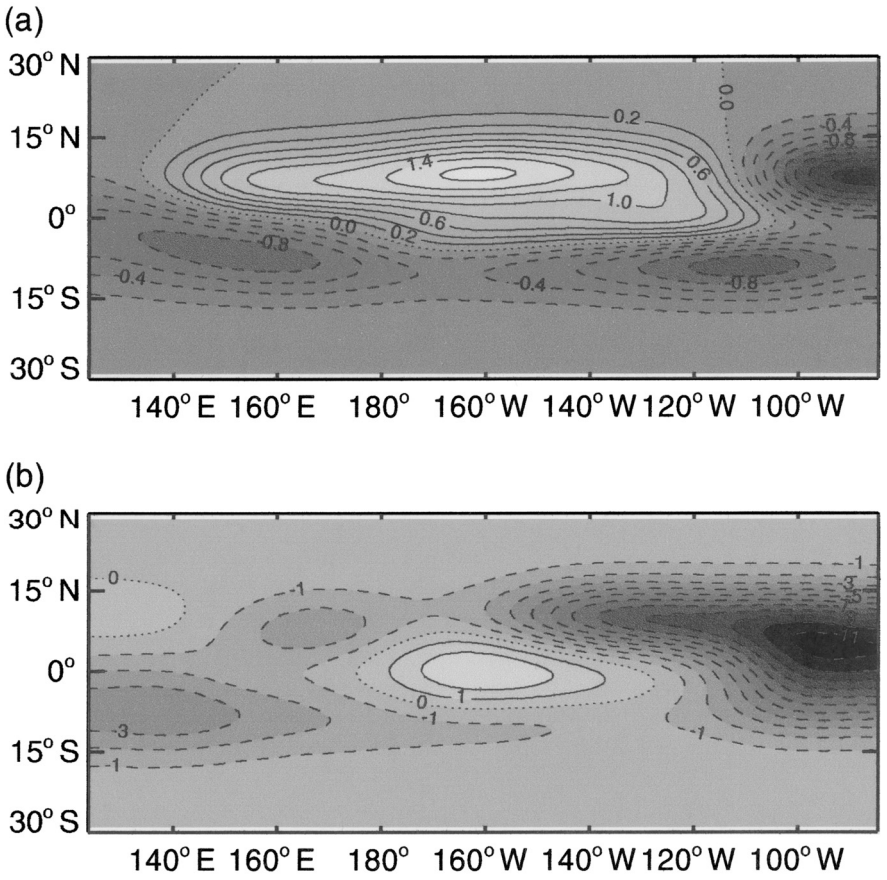


Figure 7. Initial temperature residuals: (a) weak constraint inversion (Exp. W), layer 5, min $= -1.7$ K, max $= 1.7$ K, interval $= 0.2$ K; (b) strong constraint inversion (Exp. S), layer 7, min $= -11.5$ K, max $= 2.9$ K, interval $= 1.0$ K.

the horizontal coordinates. All the penalties are dimensionless, by virtue of their respective weightings. There are no residuals in the initial layer thicknesses, since the first–guess initial conditions for thicknesses have been imposed as strong constraints. There is a significant penalty for temperature, peaked at level 9 (or a nominal depth of 140 m). The total for all layers and all variables is $\hat{\mathcal{J}}_{init} = 731$, which may be compared with the expected value $E\{\hat{\mathcal{J}}_{model}\} = E\{\hat{\mathcal{J}}_{dyn}\} + E\{\hat{\mathcal{J}}_{init}\} = 375$. Separate computation of $E\{\hat{\mathcal{J}}_{dyn}\}$ and $E\{\hat{\mathcal{J}}_{init}\}$ is extremely expensive and has not been carried out. Nevertheless, it may be concluded that even the prior estimate of 100% error in the initial temperature (see Section 3b) is exceedingly optimistic. These initial conditions, it may be recalled, were the final values of a 5 year long spin-up from rest, driven by NCEP/NCAR and FSU surface fluxes. Shown in Figure 7 are the initial temperature residuals for (a) layer 5 in the weak inversion Exp. W

and (b) layer 7 in the strong inversion Exp. S. The chosen layers have the largest residuals; the extrema in the layers are (a) 1.7 K, −1.7 K; (b) 2.9 K, −11.5 K. Note in particular the absurd minimum residual of −11.5 K introduced by the strong inversion.

*c. Dynamical residuals*

The inverse penalties in Exp. W for the zonal momentum equation, the meridional momentum equation and the temperature equation for selected layers are shown in Figures 8 a–c, as functions of time in days, integrated over the entire horizontal domain. Again, all the penalties are dimensionless, by virtue of their respective weightings. There are no residuals for the continuity equations for layer thickness, since the equations are imposed as strong constraints. The penalties shown in Figures 8 a–c all vanish at $t = 90$ days, since the weighted residuals (the adjoint variables) all vanish at that time as an Euler-Lagrange or extremal condition. In layer 1 (and layer 2, not shown) the dominant penalty is that for the temperature equation. In layer 3 (and layers 4–6, not shown), the zonal momentum penalty is dominant. This residual must be a modification to the meridional pressure gradient, consistent with the observed meridional variations in temperature. In layer 7 (and layers 8–21, not shown) only the temperature equation penalty is significant, since the momentum equations are effectively strong constraints in the deepest layers: see the vertical profiles of prior error covariances in Figure 14. The 90-day time-integrals are shown in Figure 9, layer by layer. The totals for the three equations for $(u, v, T)$, summed over all layers and all time are (523, 30, 581). Their grand total is $\hat{\mathcal{J}}_{dyn} = 1134$. The expected value is $E\{\hat{\mathcal{J}}_{dyn}\} \leq E\{\hat{\mathcal{J}}_{model}\} = 375$, with a standard deviation of $\sqrt{var\{\hat{\mathcal{J}}_{dyn}\}} \leq \sqrt{var\{\hat{\mathcal{J}}_{model}\}} = 25$, thus the seemingly very conservative (large) first–guess estimates of dynamical error are not conservative enough; a variance rescaling by $1134/375 = 3.0$ is in order.

The inverse dynamical penalties in the surface layer, for the strong constraint inversion (Exp. S; not shown) are far larger than the corresponding weak constraint penalties (Exp. W, shown in Figure 8c). Specifically, the surface layer penalties for zonal momentum, meridional momentum and heat in Exp. S exceed those in Exp. W by factors of up to 50, 5 and 2 respectively. Recall that only the surface layer dynamics in Exp. S are weak, since that layer includes the surface fluxes of momentum and heat; the dynamics of all other layers in Exp. S are strong. The zonal momentum residuals in the surface layer, for Exp. W and S, are shown in Figure 10 for Day 60: November 1, 1997. What are, in effect, excessive surface fluxes of zonal momentum in Exp. S lead to partial geostrophic balance of deep meridional temperature gradients in fair agreement with the deep TAO data. The alternative found in Exp. W, namely, moderate increases in heat flux divergences at depth, achieves better agreement.

*d. Dynamical balances*

The dominant processes in the heat equation are shown in Figure 11 (Exp. W). These are layer–by–layer profiles for a selected day (Day 15: September 15, 1997), and for a

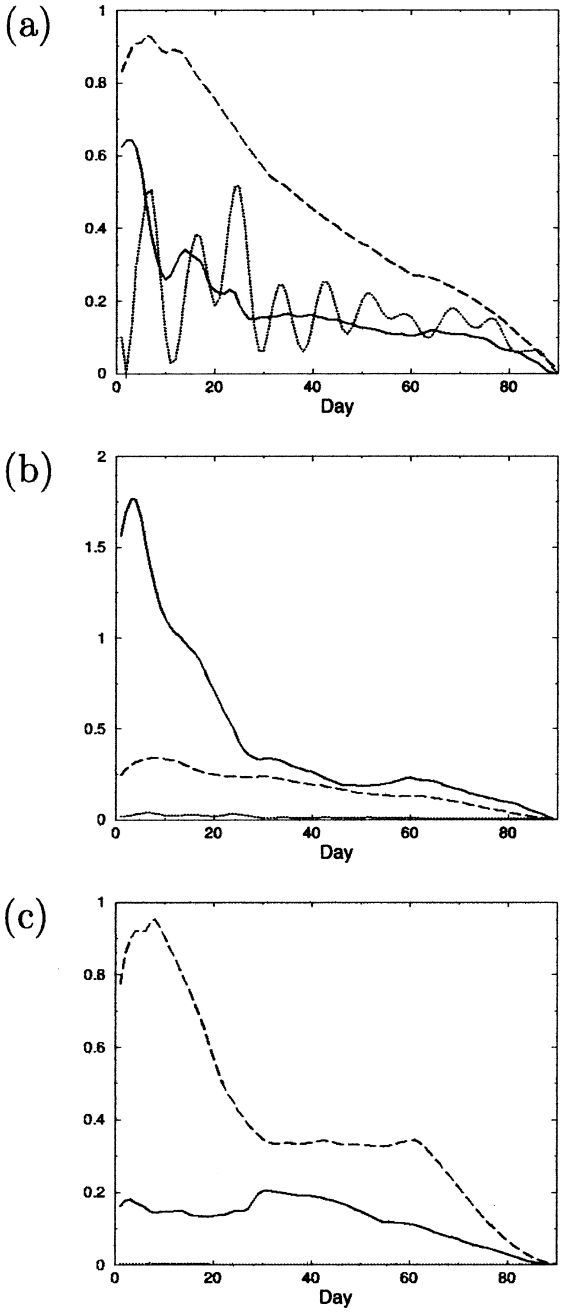


Figure 8. Time series of inverse dynamical penalty $\hat{\mathcal{J}}_{dyn}$, totalled over the horizontal. Solid line: zonal velocity. Dotted line: meridional velocity. Dashed line: temperature. (a) Layer 1; (b) Layer 3; (c) Layer 6.

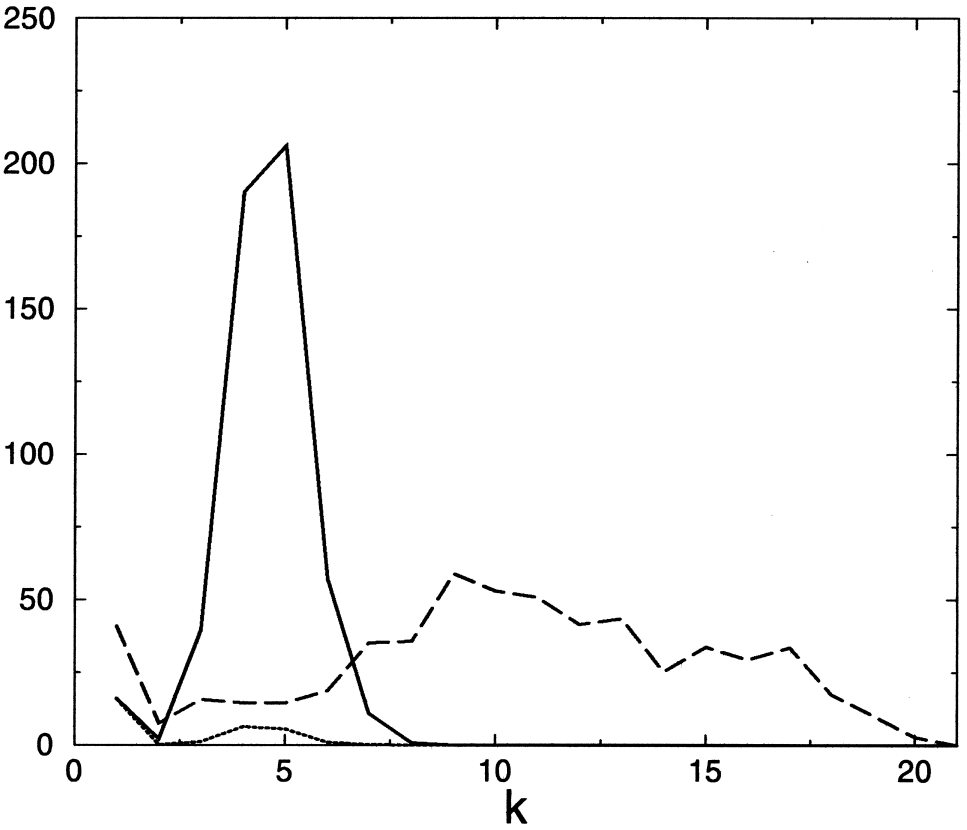


Figure 9. Vertical profiles of inverse dynamical penalty $\hat{\mathcal{J}}_{dyn}$, totalled over the horizontal and time. Solid line: zonal velocity. Dotted line: meridional velocity. Dashed line: temperature.

selected TAO array mooring site at (125W, 2N). The values have been joined with straight line segments for clarity, and plotted against depth $z$. The long dashed lines are the hypothesized standard deviations for the heat equation errors. The dominant processes above 50 m are the time rate of change $\left(\frac{\partial T}{\partial t}\right)$, the horizontal advection $(\mathbf{u} \cdot \nabla T)$, and the negative of the Richardson–number–dependent parameterization of turbulent heat flux in the vertical ($-$KPP). These processes do not balance above 10 m, where there is a significant residual ($r_T = \hat{f}_T$, where the hat denotes the optimal or inverse value). Again, the mixed layer depth has been set to 10 m and only the 'KPP-interior' parameterization has been used. Between 50 m and 200 m, the dominant processes are primarily the time rate of change $\left(\frac{\partial T}{\partial t}\right)$, and the vertical advection $\left(w\frac{\partial T}{\partial z}\right)$, and secondarily the horizontal advection $(\mathbf{u} \cdot \nabla T)$. There is a significant residual $(r_T)$ between 130 m and 160 m. Below 200 m, all processes are insignificant relative to the hypothesized error.

The dominant processes in the zonal momentum equation are shown in Figure 12. These are values for Day 15, for the TAO array mooring site at (155W, 8N), layer by layer as

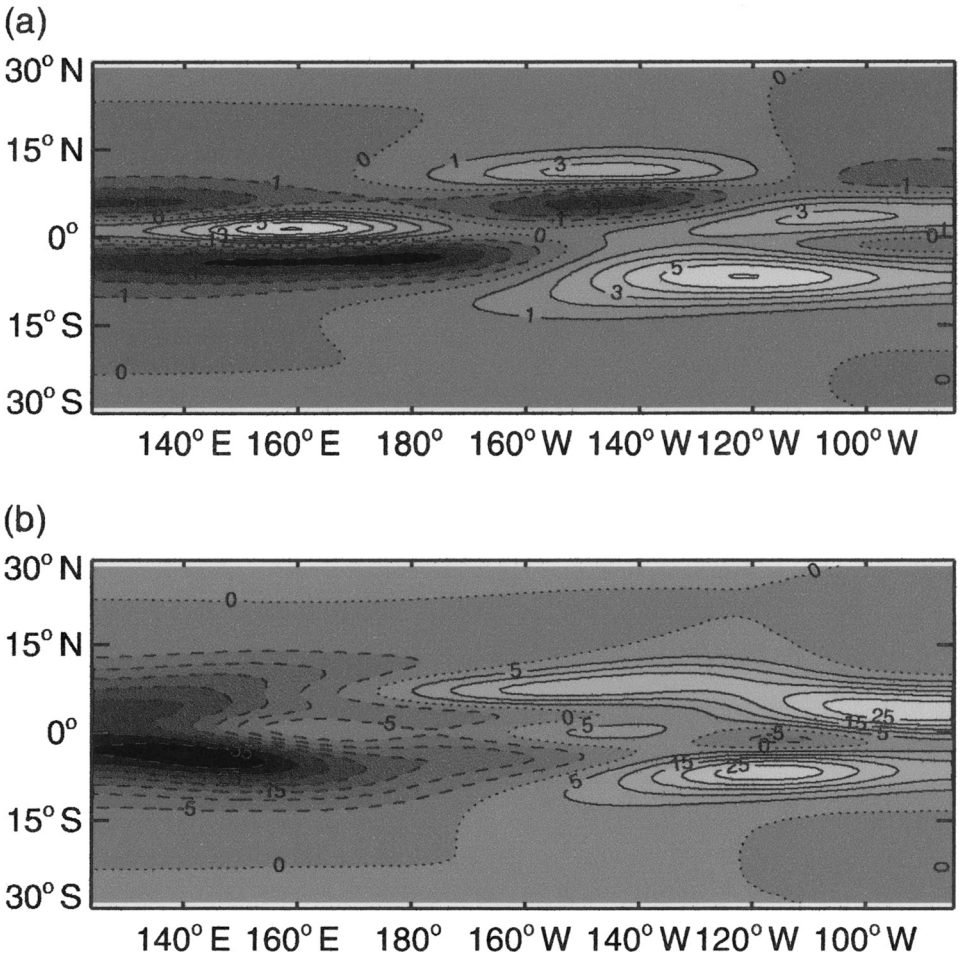


Figure 10. Residuals in the surface layer equation for zonal momentum, Day 60 (November 1, 1997). Units are: $10^{-7}\,\mathrm{m\,s^{-2}}$. (a) Exp. W: weak dynamics in every layer; min $= -4.4$, max $= 6.0$, interval $= 1.0$. (b) Exp. S: weak dynamics in the surface layer only; min $= -40.0$, max $= 29.0$, interval $= 5.0$.

in Figure 11. There is a residual $r_u = \hat{f}_u$ between 40 m and 100 m, but it lies within the hypothesized standard error. At all depths, the dominant processes are the zonal acceleration $\left(\frac{\partial u}{\partial t}\right)$ and the Coriolis acceleration $(-\beta y v)$.

In a conventional analysis, these dynamical balances would be investigated for the presence of meridional circulation, Tropical Instability Waves, equatorial Kelvin waves or Rossby waves. The significance of the meridional velocity does not of course preclude the presence of Kelvin waves here in this potentially mixed wave field. On the other hand, the insignificance of the zonal pressure gradient does tend to preclude Kelvin waves. Yet, as Stommel points out (Stommel, 1989), free wave solutions are in general inadequate

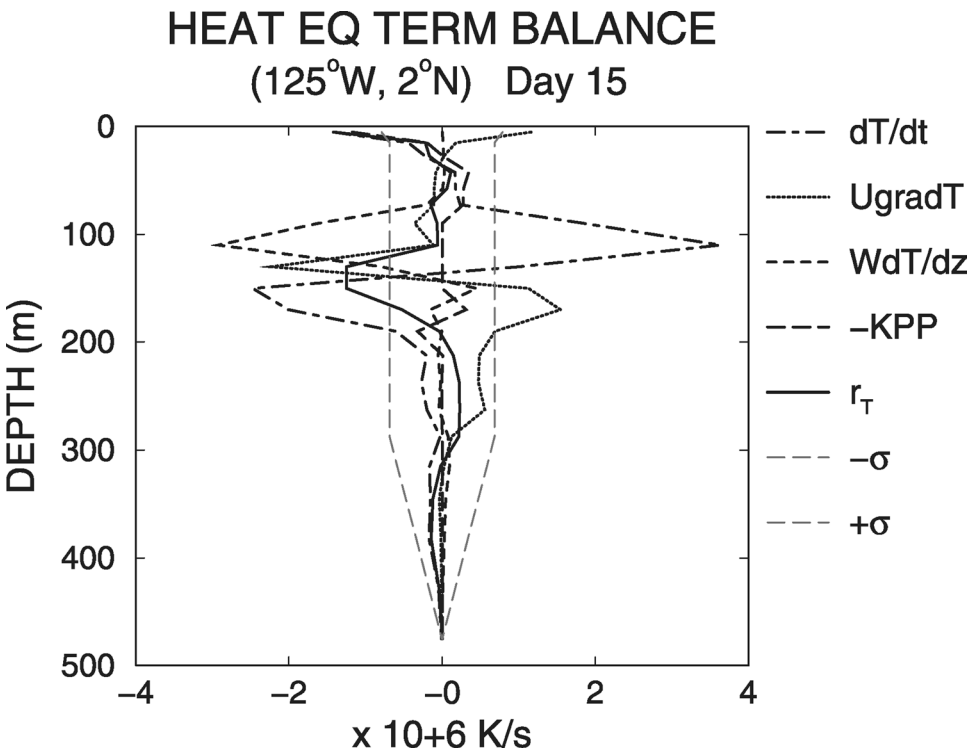


Figure 11. Vertical profiles of the dynamical balance for temperature at (125W, 2N) on Day 15. Units are: $10^{-6}$ K s$^{-1}$. The long dashed lines are the hypothesized standard deviations $\pm\sigma_T$ for the dynamical residual $r_T$. Only significant terms in the balance are plotted. The ordinary derivatives indicated in the legend are in fact partials.

characterizations of real ocean circulation; it is argued elsewhere (Bennett, 1992, 2002) that the rational characterization is in terms of the modes of circulation observable by the array, here the TAO array. These array modes are *forced* solutions of the equations of motion. We omit such a characterization here in the interests of brevity.

Mindful of Stommel's warning, we nevertheless offer a conventional analysis of the optimal dynamical balances. The meridional momentum balance (not shown) is approximately geostrophic, as is expected for these long–wave, equatorially confined, subinertial motions. The vertical momentum balance is hydrostatic by assumption, and volume is conserved in a Boussinesq fluid (Phillips, 1966). It is a textbook exercise to show that these primary balances (including those seen in Figs. 11 and 12) admit travelling disturbances confined to the upper ocean, with the meridional velocity having the functional form

$$v(x, y, z, t) \sim \sin[\kappa(x + ct)] \exp[-nz] V(y), \tag{5}$$

where $\kappa$ is an unspecified zonal wavenumber and $n$ an unspecified but positive vertical length scale. The function $V(y)$ is related to the parabolic cylinder functions (Abramowitz

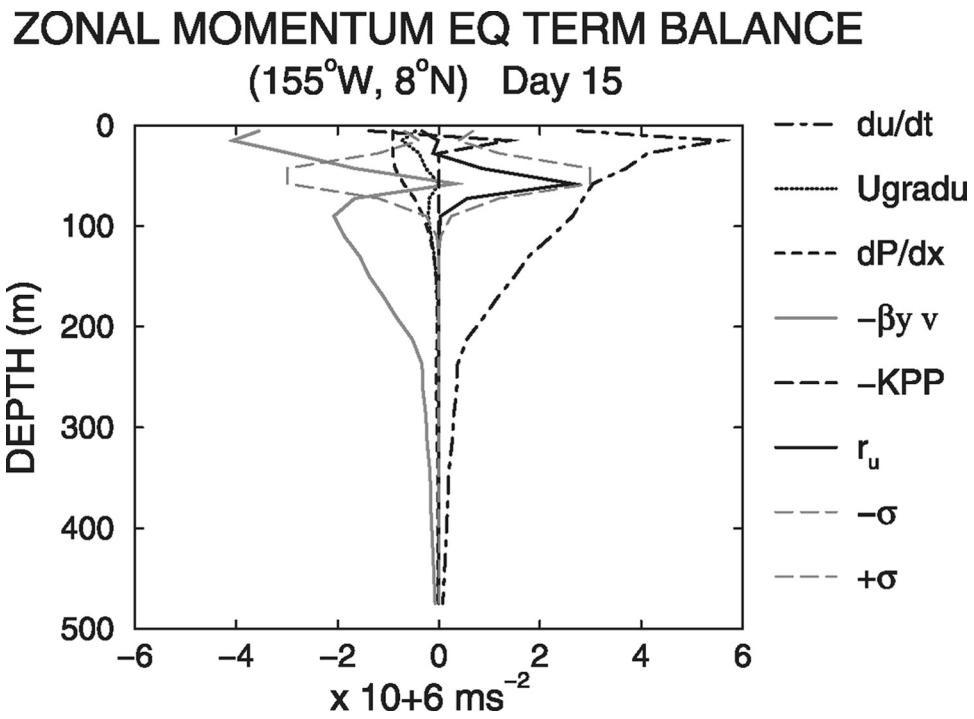


Figure 12. Vertical profiles of the dynamical balance for zonal momentum at (155W, 8N), Day 15 (September 15, 1997). Units are: $10^{-6}$ m s$^{-2}$. The long dashed lines are the hypothesized standard deviations $\pm\sigma_u$ for the dynamical residual $r_u$. Only significant terms in the balance are plotted. The ordinary derivatives indicated in the legend are in fact partials.

and Stegun, 1964). The meridional length scales appearing in $V$ are the decay scale $\sqrt{c/\beta}$ and the oscillation scale $\sqrt{N/(\beta n)}$, where $N$ is the Nyquist freqency (Phillips, 1966). The other components of velocity, and the thermodynamic variables, have similar forms. The disturbances are equatorially confined ($V \to 0$, as $|y| \to \infty$) provided the phase speed $c$ is positive, that is, if the zonal propagation is westward. In other words, the dynamical balances that support the optimal fits to the data also admit familiar and simple patterns of equatorial circulation (e.g., Philander, 1990). Indeed, the optimal estimate of the equatorial circulation manifests many of the features of (5), as well as those of the hypothesized error covariances that shape the dynamical residuals. The climatological choices (Tables 4 and 5) for the scales of the covariances are consistent with the approximate dynamical balances seen in Figures 11 and 12. The optimal fit to the TAO observations is an unexceptionable estimate of the ocean state.

*e. Degrees of freedom*

There would seem to be a conflict between the unexpectedly large values of the dynamical penalties (see Tables 2, 3) and the moderate values of the residuals in the equations of motion. There was no such conflict for the coupled intermediate model investigated by

Table 4. Standard deviations and decorrelation scales for dynamical residuals. Layers are assumed to be uncorrelated.

| Dynamical residuals | Standard deviation σ | Zonal scale $L_x$ | Meridional scale $L_y$ | Time scale τ |
|---|---|---|---|---|
| $f_u$, $f_v$ (surface) | see Fig. 15 | $3 \times 10^6$ m | $5 \times 10^5$ m | $2.5 \times 10^6$ s |
| $f_u$, $f_v$ (subsurface) | see Fig. 15 | $10^6$ m | $2.5 \times 10^5$ m | $5 \times 10^5$ s |
| $f_T$ (surface) | see Fig. 15 | $3 \times 10^6$ m | $5 \times 10^5$ m | $2.5 \times 10^6$ s |
| $f_T$ (subsurface) | see Fig. 15 | $10^6$ m | $10^6$ m | $5 \times 10^5$ s |
| $f_h$ | $4 \times 10^{-7}$ m s$^{-1}$ | $10^6$ m | $10^6$ m | $5 \times 10^5$ s |

Bennett *et al.*, (1998, 2000); both total penalties and pointwise residuals were significantly too large. A scale analysis indicates that there is no inconsistency here. For example, the total dynamical penalty for the temperature is approximately

$$\mathcal{J}_T = \left(\frac{f_T}{\sigma_T}\right)^2 \frac{XYZt_{\max}}{L_x L_y L_z \tau} \tag{6}$$

where $X$, $Y$, $Z$, $t_{\max}$ are the ranges for $x$, $y$, $z$ and $t$, while $L_x$, $L_y$, $L_z$ and τ are the decorrelation scales for the residual $f_T$ in the heat equation. The scale estimate (6) is not immediately obvious: as is shown in Chua and Bennett (2001) and Bennett (2002), the weights in the penalty are related to the hypothesized error covariances through integral equations. To continue, (6) may be written $\hat{\mathcal{J}}_T = \left(\frac{f_T}{\sigma_T}\right)^2 N_T$, where $N_T$ is the effective number of degrees of freedom in the dynamical residual within the four dimensional domain. The error correlation scales define internally correlated residual 'blobs' in 4D; the number of such blobs in the 4D domain of the model is the effective number of controls on the circulation. It is intuitively clear that if there are many more blobs than there are data, then a good fit to the dynamics, initial conditions and data may be feasible even if the error hypothesis is wrong.

The relationship between the test statistic and the residuals is illustrated here using a multi-dimensional algebraic least squares problem. Let $\mathbf{U}$ be a state vector in $\mathbb{R}^N$. For simplicity, the dynamical model is chosen to be the unit matrix:

$$\mathbf{U} = \mathbf{F} + \mathbf{f} \tag{7}$$

where $\mathbf{F}$ is the first–guess forcing and $\mathbf{f}$ the first–guess forcing error. In particular, $\mathbf{U}_F = \mathbf{F}$. The data are

$$\mathbf{d} = \mathbf{M}\mathbf{U} + \boldsymbol{\epsilon} \tag{8}$$

Table 5. Standard deviations and decorrelation scales for initial residuals. Layers are assumed to be uncorrelated.

| Initial residuals | Standard deviation σ | Zonal scale $L_x$ | Meridional scale $L_y$ |
|---|---|---|---|
| $u$, $v$ (above 50 m) | see Fig. 13 | $10^6$ m | $2.5 \times 10^5$ m |
| $u$, $v$ (below 50 m) | see Fig. 13 | $3 \times 10^6$ m | $5 \times 10^5$ m |
| $T$ | see Fig. 14 | $10^6$ m | $10^6$ m$ |
| $h_T$ | 25 m | $3 \times 10^6$ m | $5 \times 10^5$ m |

where $\mathbf{d} \in \mathbb{R}^M$. For simplicity, the linear measurement operator $\mathbf{M}$ is chosen to be a projection: the first $M$ rows of the $N \times N$ identity matrix $\mathbf{I}_{N\times N}$ and hence $\mathbf{M}\mathbf{M}^T = \mathbf{I}_{M\times M}$. The measurement error is $\boldsymbol{\epsilon}$. For simplicity the estimator or penalty is chosen to be diagonal:

$$\begin{aligned}\mathcal{J}[\mathbf{U}] &= \frac{\mathbf{f}^T\mathbf{f}}{\sigma_f^2} + \frac{\boldsymbol{\epsilon}^T\boldsymbol{\epsilon}}{\sigma_\epsilon^2} \\ &= \frac{(\mathbf{U}-\mathbf{F})^T(\mathbf{U}-\mathbf{F})}{\sigma_f^2} + \frac{(\mathbf{d}-\mathbf{M}\mathbf{U})^T(\mathbf{d}-\mathbf{M}\mathbf{U})}{\sigma_\epsilon^2}. \end{aligned} \tag{9}$$

The hypothesis is that the model possesses $N$ uncorrelated degrees of freedom each having the variance $\sigma_f^2$, while there are $M$ data with uncorrelated errors each having the variance $\sigma_\epsilon^2$. The extremum of $\mathcal{J}$ is

$$\hat{\mathbf{U}} = \mathbf{F} + \sigma_f^2 \mathbf{M}^T \hat{\boldsymbol{\beta}}, \tag{10}$$

since the $M$ 'representers' are just the $M$ rows of $\sigma_f^2\mathbf{M}$. The representer coefficients $\hat{\boldsymbol{\beta}}$ are

$$\hat{\boldsymbol{\beta}} = \frac{\mathbf{h}}{\sigma_f^2 + \sigma_\epsilon^2}, \tag{11}$$

where $\mathbf{h} \equiv \mathbf{d} - \mathbf{M}\mathbf{F}$. It is readily shown that

$$\hat{\mathcal{J}} = \mathcal{J}[\hat{\mathbf{U}}] = \hat{\mathcal{J}}_{model} + \hat{\mathcal{J}}_{data} = \hat{\mathcal{J}}\frac{\sigma_f^2}{\sigma_f^2+\sigma_\epsilon^2} + \hat{\mathcal{J}}\frac{\sigma_\epsilon^2}{\sigma_f^2+\sigma_\epsilon^2} = \frac{\mathbf{h}^T\mathbf{h}}{\sigma_f^2+\sigma_\epsilon^2}. \tag{12}$$

The total model residual is

$$(\hat{\mathbf{U}}-\mathbf{F})^T(\hat{\mathbf{U}}-\mathbf{F}) = \sigma_f^2\hat{\mathcal{J}}_{model} = \hat{\mathcal{J}}\frac{\sigma_f^4}{\sigma_f^2+\sigma_\epsilon^2}. \tag{13}$$

Note that the null hypothesis implies $E\{\mathbf{h}\mathbf{h}^T\} = (\sigma_f^2+\sigma_\epsilon^2)\mathbf{I}$. In particular, $E\{\mathbf{h}\mathbf{h}^T\} = M(\sigma_f^2+\sigma_\epsilon^2)$, $E\{\hat{\mathcal{J}}\} = M$ and $var\{\hat{\mathcal{J}}\} = 2M$. Suppose, as is approximately the case for Exp. W, that $\hat{\mathcal{J}}_{model} = \hat{\mathcal{J}}_{data} = \frac{1}{2}\hat{\mathcal{J}} = M$. It must be the case that $\sigma_f^2 = \sigma_\epsilon^2$, and so the rms model residual component is

$$\sqrt{\frac{(\hat{\mathbf{U}}-\mathbf{F})^T(\hat{\mathbf{U}}-\mathbf{F})}{N}} = \sqrt{\frac{M}{N}}\sigma_f. \tag{14}$$

Thus, while there are only $M$ degrees of freedom in the 'data subspace' of the state space $\mathbb{R}^N$ (in which subspace the inverse lies: see e.g., Bennett, 1992), the variance in each degree of freedom is shared by $N$ components or blobs. Thus, pointwise presentation of residuals as in Figures 11, 12 can be misleading when the presentation indicates relatively small residuals. When the number $M$ of data (and hence the number of observable degrees of freedom) is far less than the number $N$ of degrees of freedom in the state space (data subspace *plus*

null subspace), the pointwise residuals $r_n = \hat{f}_n = \hat{U}_n - F_n$ and data misfits $\hat{\epsilon}_n$ can be small ($|r_n| < \sigma_f$, $1 \leq n \leq N$; $|\hat{\epsilon}_m| \leq \sigma_\epsilon$, $1 \leq m \leq M$) but the test statistic is not misled ($\hat{\mathcal{J}} - M \gg \sqrt{2M}$).

For a 90-day inversion, and remembering that there are residuals in the dynamics of zonal velocity, meridional velocity and temperature, the number of residual degrees of freedom is approximately $N = 30{,}000$. The number of data is approximately $M = 2{,}000$, so $(M/N)^{1/2} \cong 1/4$, thus (14) is roughly consistent with the residuals in Exp. W: see Figure 11. Dynamical residuals for velocity have less impact upon the temperature than do the dynamical residuals for temperature, so the preceding numerical estimate for the effective number of degrees of freedom $N$ tends to be excessive on the one hand; on the other, velocity residuals are likely to be relatively larger than temperature residuals: see Figure 12. The value of $N$ is particularly large owing to the assumption that the dynamical residuals are uncorrelated in the vertical, which has been discretized here into 21 layers. The assumption would seem excessive, as the ENSO thermal variability in the circulation can be efficiently represented with two or three vertical modes. However, what is at issue here is the number of modes in the error in the parameterization of vertical fluxes. Our almost total lack of knowledge of this number motivated us to be as generous as possible to the Gent–Cane model, by admitting as many residual degrees of freedom in the vertical as possible. Assuming only two or three degrees of freedom would have been effectively the same as replacing the inverse Gent–Cane ocean model with the inverse intermediate-model ocean of Bennett *et al.* (1998, 2000). The latter is a variant of the Cane–Zebiak model, and has only $2\frac{1}{2}$ oceanic layers and which requires unacceptably large residuals in order to fit just the SST and 20 C isotherm depth. The SST data and the subsurface temperature data at the 8 or 9 depths included here would have been even more difficult to fit.

We infer that these Gent–Cane inversions fit the observations closely with modest residuals in the dynamics, not because the hypothesized errors are far too conservative (too big), but simply because there are so many more degrees of freedom in the dynamical residuals than in the data. The weighted least squares estimator $\mathcal{J}$ correctly takes into account the number of degrees of freedom in both. Its reduced value $\hat{\mathcal{J}}$ is the appropriate test statistic, and the reduced values clearly indicate that the hypothesized errors are in fact optimistic (too small). Also, the paucity of monthly mean TAO data relative to the number of degrees of freedom in the inverse model does not prevent an objective test of the model.

The 'uncorrelated' estimator (9) which simplified this analysis is not less general than an estimator for correlated residuals, since the vector of dynamical residuals may be projected onto the eigenvectors of the dynamical error covariance matrix. Equally, the covariance for the data residuals may be independently diagonalized. Moreover, the 'identity' model operator in (7) is not less general than any well-posed model operator. Finally, it should also be noted that this entire critique of model residuals has been kind. If the null hypothesis were sound, the residuals would be smaller than their inverse or *posterior* standard deviations, which are smaller than the first guesses or *priors*: see e.g., Bennett (1992).

## 6. Summary and discussion

Previous long–term integrations of the reduced–gravity tropical circulation model of Gent and Cane (1989), forced by monthly mean climatological surface fluxes, lead to annual average equatorial SST which is 'quite realistic' (Gent, 1991). The model has been tested here by attempting to reconcile it with high quality surface and subsurface monthly mean measurements of ocean temperature collected by the TAO array. That is, the smallest residuals in the equations of motion and surface fluxes (FSU pseudo stresses and NCEP/NCAR reanalyzed heat fluxes) have been sought consistent with the monthly mean TAO data. The residuals are smallest in the sense of yielding weighted least-squares best fits simultaneously to the dynamics, initial conditions and data; the weights are inverses of the hypothesized error covariances for each constraint. First–guess means and autocovariances for the errors are based on climatology, and on direct measurements of subsurface flux profiles. The subsurface flux parameterizations using the KPP interior scheme have been assumed 100 % in error. By 'Gent–Cane model' we mean not only the equations of motion and the supply of inputs, but also the hypothesized errors in all this structure. The essential features of our detailed hypothesis are simple and robust: significant levels of error are assumed in the dynamical and initial constraints, and the decorrelation scales imply that there are a large number of effective degrees of freedom in the errors or constraint residuals. We have tested the combined hypothesis in a standard way, that is, by minimizing the associated estimator of maximum likelihood. This minimization process is also the generalized inversion of the overdetermined system of equations of motion, initial conditions, boundary conditions and data.

Our first finding is that the 'forward' Gent–Cane model only yields a general resemblence to the TAO data ($\pm 3$ K) if there are at least $21\frac{1}{2}$ model layers. We therefore caution against the general use of the model at lower resolution; all the inverse model experiments reported here use this minimal acceptable resolution.

Unlike the inversions of the Cane–Zebiak–like intermediate anomaly model with its linearized continuity equations (Bennett *et al.*, 1998, 2000), but like the inversions of a $2\frac{1}{2}$ layer primitive equation model (Ngodock *et al.*, 2000), the iterations on the nonlinear Euler–Lagrange equations for the best fit to the $21\frac{1}{2}$–layer Gent–Cane model and TAO data over twelve months do not converge owing to outcropping of the deep bounding isotherm. We speculate from other experience that more observations of the depth of this isotherm would keep it under control. In the absence of a sufficiency of high–quality, regularly spaced but unbinned data for the depth of the bounding isotherm, convergence of our algorithm has been obtained by imposing the continuity equation for the deep bounding isotherm, and the initial depth of the isotherm, as strong constraints (allowing no residuals), and by restricting the inversions to intervals of three months. We have reported in detail the inversion that shows the model in the best light.

The best inversion fits the data within monthly–mean observational error. Moreover, the residuals for the momentum equations and internal energy equations are not only smaller than the respective first–guess standard errors, but play only modest roles in the dynamical balances. We have therefore achieved the operational objective of a four–dimensional ocean

analysis of real surface fluxes and real subsurface data, fairly closely constrained by an appropriately complete model of tropical Pacific circulation. This is as valuable an analysis as is presently available. Nevertheless, the significance tests for the inversion indicate that the reanalysis has a low probability and that if more data were available, such good fits to the data could only be obtained by admitting model residuals in excess of their hypothesized values. A rescaling of the hypothesized variances would be of little scientific value, as the dynamical constraints would be close to becoming slack. There is a simple explanation for the seeming paradox of locally–small residuals and large posterior penalties: the number of effective degrees of freedom in the weak constraint model, especially in the vertical, greatly exceeds the existing number of monthly mean TAO surface and subsurface data. Thus an excellent data fit can be obtained, with locally–small dynamical residual variance shared over the many effective degrees of freedom. However, the test statistic is not misled since it properly tallies the effective degrees of freedom. Thus we pause before affirming Stommel's conclusion: *The plausible hypothesis must be tested by specifically designed observations*, since we have been able test and reject a model with an independently–designed data set. Nevertheless, affirmation of our conclusion: *the model would be unable to fit data having greater vertical resolution*, requires either additional vertical resolution in the mooring data, or profile data from, say, the ARGO floats (`http://www.argo.ucsd.edu/`).

Some previous assessments of ocean models for El Niño events have compared the realism of solutions driven by four or five different analyses of the surface wind in the same event. Harrison *et al.* (1989) employ the Primitive–Equation ocean model of Philander and Siegel (1985), and abstract their findings as follows. *Comparing the hindcasts with (ship–of–opportunity expendable bathythermograph) observations, we find that the gross large–scale changes of the ENSO event… are found in each hindcast. However, major quantitative differences exist between each hindcast and the observations in at least some region for some time and some variable*. Hackert *et al.* (2001) use a $19\frac{1}{2}$–layer Gent–Cane model, with remotely–sensed winds as well as NWP–based analyses. Their findings may be summarized similarly. Harrison *et al.* (1989) draw the following striking conclusions. *In almost every comparison, the range of hindcast results brackets the observations, suggesting that the (Philander and Siegel, 1985) model physics is plausible…. Improved knowledge of the surface wind stress field (and its curl) is a minimum requirement if we are to assess more critically model performance, and to identify needed model performance*.

In comparison, the optimally perturbed model here fits the observations within observational error. Moreover, the perturbations which minimize the data misfits are themselves of insignificant amplitude, point–by–point. The Monte–Carlo simulations also reported here strongly indicate that in fact a very large number of perturbations or samples is needed for an effective direct exploration of the error space. The indirect search for an optimum via a variational algorithm is admittedly expensive, but a maximum–likelihood estimate is found. The standard regression analysis used here establishes that the seemingly good fit is in fact statistically unreliable, owing to an excess of degrees of freedom in the control space (the number of space–time correlated 'blobs' in the subsurface flux residuals). Our conclusion

may seem to be at odds with Harrison *et al.* (1989). In the strictest of terms, we conclude that a four–dimensional analysis of TAO data using the Gent–Cane model must allow for significant errors in the subsurface fluxes; perturbations of the surface wind fields are less effective at controlling the subsurface temperatures. On the other hand, the TAO subsurface data cannot identify wind field errors in the null space of the array; the first–guess wind analysis should of course be as good as possible.[6]

Intermediate coupled models have been used recently by Morss and Battisti (2004a,b) for the design of ENSO observing systems. Those authors caution that "*the results are only applicable to the real world to the extent that the simulated system is an adequate representation of the real system.*" We concur, and add to our earlier caution by warning against the use of this reduced–gravity model, or the intermediate coupled models also rejected by inversions with TAO data, for the design of observing arrays. We add further that, of course, an ocean model must be tested with real ocean data if it is to be used to design observing arrays. On the other hand, the observing array that provides the test data cannot be designed without an hypothesis about the circulation that is to be observed, that is, without an ocean model. Ocean array design and ocean model testing are inextricably intertwined. The generalized inversion of an ocean model, as performed here, simultaneously tests the ocean model and reveals the conditioning or efficiency of arrays for observing the hypothesized circulation.

This test of the Gent–Cane model is made with data from the 1997–98 El Niño. Our experience with an intermediate coupled model has been equally clear rejection of that model by TAO data for the moderate 1994–95 El Niño, the mild 1995–96 La Niña and the very strong 1997–98 El Niño. We infer that the conclusions of this test of the Gent–Cane model are not limited to any one climate state.

The suspected fault in the hypothesized model surely must result from our poor understanding of errors in surface and subsurface flux parameterizations—especially the latter in the vertical direction—rather than to the underlying hydrodynamical assumptions (Boussinesq fluid, hydrostatic approximation, reduced gravity, etc). It is implausible that filtering the barotropic mode is a primary model flaw, but the possibility cannot be tested with this model, nor with the data available to us. The vertical distributions of prior and posterior temperature errors (Fig. 3) strongly indicate that the fault lies in the parameterized subsurface fluxes rather than in the reanalysed surface fluxes or in the assumption of a fixed mixed–layer depth. Neverthless, we infer the need for more knowledge of the biases and the spatial and temporal covariances of errors in all flux parameterizations. Of course, it would even more desirable to have better parameterizations, or in other words, to solve the problem of stratified turbulence. But inverse modeling (and in particular, hypothesis testing) would benefit greatly just from more reliable quantitative bounds on the problem, be they observational or theoretical. That is, we would benefit from better parameterization

6. Wind perturbations are in the null space for the thermal array if those perturbations lead, via the ocean dynamics, to no changes in measured temperatures.

error statistics. It might be concluded that what has been tested here is the KPP interior parameterization scheme rather than the pseudolaminar dynamics of the Gent–Cane model itself, since the KPP scheme is used here as a basis for formulating error priors. However, the inversions show that the Gent–Cane model may be fit to the data by allowing locally marginally insignificant dynamical residuals of unspecified origin. On the other hand, the very significantly large number of energetic degrees allowed in the error field is critical to the good fit, regardless of the source of error.

Finally, it is necessary to consider that the scaled vertical coordinate in the Gent–Cane model may not in fact lead to adequate numerical resolution in the seasonal thermocline and shallower. The accuracy of the horizontal pressure gradient is of concern in any model with a nonuniformly stretched vertical coordinate (Haidvogel and Beckmann, 1999). However, the numerical resolution employed here in all directions should resolve the monthly–mean equatorial circulation. Preliminary forward integrations with a standard, level–coordinate, Primitive–Equation model having the same nominal vertical resolution as used here, and forced by identical surface fluxes, do yield fractionally more accurate first–guess solutions, but the subsurface flux parameterizations remain as the principal suspects.

A great deal of intricate code is needed for the implementation of the generalized inverse algorithm and diagnostics employed here, beyond even the development of an adjoint ocean model. However, the code is freely available as a model–independent or modular system (the 'Inverse Ocean Modeling' system, or IOM). The code is accessed and executed via a graphical user interface that prompts for paths, information about data structures, run–time environment, etc. Several community ocean models already conform to the IOM protocols.[7]

*Acknowledgments.* Our work at Oregon State University has been supported by NCEP and ONR through the Visiting Scientist Programs of the University Corporation for Atmospheric Research, by NSF (OCE-9520956, OCE-0121542) and by ONR (N00014-99-1-00-49). All the computations were performed on the COAS CM-5 and CM-500e systems. The COAS CM-5 is supported by NASA EOS; we are grateful to Mark Abbott for access to it, and to his research associate Curt Vandetta for servicing all the 'CMs.' The COAS CM-500e systems were donated by the Office of Naval Research, via NSF . The TAO data were kindly prepared and provided by Dai McClurg of NOAA/PMEL. MJM was supported by the NOAA Office of Oceanic and Atmospheric Research, and by the NOAA Office of Global Programs. The comments of two anonymous reviewers were very helpful. This is PMEL contribution no. 2754.

## APPENDIX A

### Global nonlinear analytic interpolation

We define the temperature measurement functional by

$$T(z) = \sum_{k=1}^{K} w_k(z) T_k \tag{15}$$

7. `http://iom.asu.edu`

where $T(z)$ is the model temperature interpolated to depth $z$, while $T_1, \ldots, T_K$ are the model temperatures on surfaces $s_1, \ldots, s_K$, with weights $w_1, \ldots, w_K$. We require that each $w_k(z)$ be smooth, and

$$\sum_{k=1}^{K} w_k(z) = 1 \tag{16}$$

for all $z$. We choose

$$w_k(z) = \frac{\exp\{-(z - z_k)^2 D^{-2}\}}{\sum_{j=1}^{K} \exp\{-(z - z_j)^2 D^{-2}\}} \tag{17}$$

where $z_1, \ldots, z_K$ are the local instantaneous depths of the surfaces $s_1, \ldots, s_K$, and $D = 25\,\text{m}$ is the nominal layer thickness (there are 21 layers spanning 500 m). Thus, (15)–(17) maps the model variables $T_k$ and $z_k$ into the 'datum' $T(z)$, but in a nonlinear fashion. The interpolation algorithm (15)–(17) reconstructs a synthetic profile representative of the tropical thermocline (an hyperbolic tangent profile from 30°C to 10°C, centered at 200 m, with a vertical scale of 50 m, sampled every 25 m) to within the 0.4 K standard error prescribed for the real monthly–mean data. Our Picard iteration (described in Section 4) replaces the nonlinear functional (15)–(17) with its tangent linearization about preceding inverse estimates of $T_k$ and $z_k$. However, (15)–(17) obtains in the limit. A piecewise linear interpolation through the layers might seem simpler but its segments, being defined by layer depths, are dependent variables. Hence such a piecewise scheme is, like the global scheme (15)–(17), functionally nonlinear but lacks the functional differentiability of the global scheme. The global scheme is in fact analytic, that is, infinitely differentiable.

## APPENDIX B

### Error correlations, variances and scales

Our knowledge of errors in turbulent flux parameterizations in the tropical Pacific Ocean is poor, so we adopt the simplest and most computationally convenient forms for the covariances hypothesized in (4). The covariances are separable with respect to all independent variables: time, the vertical and both horizontal coordinates. The covariance factor for time is stationary, and the covariance factor for the zonal coordinate is homogeneous. The meridional and vertical factors are inhomogeneous. The parameters in each factor are based on those employed in Bennett *et al.* (1998, 2000) and Ngodock *et al.* (2000), which were in turn derived from long-term TAO statistics (Kessler *et al.*, 1996). The parameter values in Bennett *et al.* (1998, 2000) relate to a model of anomalies with respect to the tropical annual cycle, and so had to be modified for the Gent–Cane total disturbance model. As in the earlier studies, pseudo surface stresses are monthly mean Florida State University (FSU) values (Legler and O'Brien, 1988); surface fluxes of heat are monthly-mean NCEP/NCAR reanalyses (Kalnay *et al.*, 1996); scale estimates for FSU and NCEP/NCAR errors are ours.

The parameters used here are listed in Tables 4 and 5. The notation $f_u$ etc. denotes the residual in the zonal momentum equation, etc.

*Temporal covariances*

Temporal covariances are assumed to be stationary, and temporal correlations $C_t$ are assumed to be Markovian:

$$C_t(t' - t'') = \exp\left[-\frac{|t' - t''|}{\tau}\right], \tag{18}$$

where $\tau$ is a decorrelation time. The stationarity assumption is dubious. ENSO is an intermittent event, possibly with trends in means and higher moments, but these moments are all poorly known. Again, the assumption concerns dynamical errors rather than the ocean state itself, and so the moments even worse known.

*Zonal covariances*

Zonal covariances are assumed to be homogeneous, and zonal correlations $C_x$ are assumed to be 'bell-shaped':

$$C_x(x' - x'') = \exp\left[-\frac{(x' - x'')^2}{L_x^2}\right], \tag{19}$$

where $L_x$ is a zonal decorrelation length.

*Meridional covariances*

Meridional covariances are assumed to be inhomogeneous. The *standard deviation* is also assumed to be 'bell-shaped':

$$\sigma_y(y) = \exp\left[\frac{-y^2}{2l_y^2}\right], \tag{20}$$

where $l_y$ is a shear length.

The meridional *correlation* $C_y$ is assumed to be 'bell-shaped':

$$C_y(y' - y'') = \exp\left[-\frac{(y' - y'')^2}{L_y^2}\right], \tag{21}$$

where $L_y$ is a meridional decorrelation length.

*Vertical covariances*

Vertical covariances are assumed to be inhomogeneous. The vertical profiles of standard deviations for the initial velocity residuals (errors in initial conditions) are plotted in

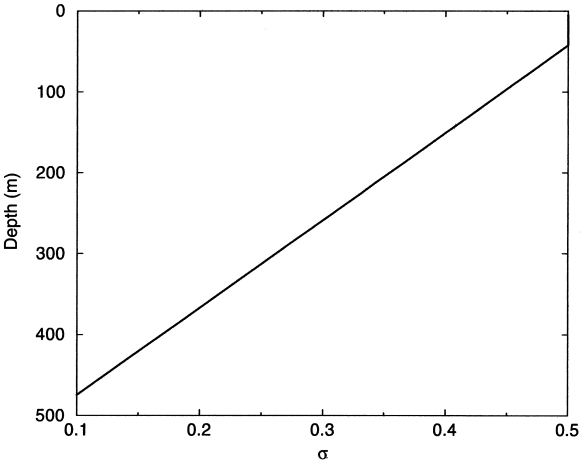


Figure 13. Vertical profile of the hypothesized standard deviation of initial velocity residual (units for $\sigma$ : m s$^{-1}$).

Figure 13. The standard errors in the initial analyses of zonal and meridional velocities are both assumed to be 100% of the NCEP/NCAR re–analysis standard deviations for those quantities (Kalnay *et al.*, 1996). That is, both standard errors are assigned the value of 0.5 m s$^{-1}$ above 50 m depth surface, decreasing linearly to zero at 450 m. The standard errors for temperature analyses are also assumed to 100%, and are equated to the TAO vertical profile of climatological, all–mooring standard deviation of temperature (Fig. 14).

The vertical standard deviations for the dynamical residuals inferred from Peters *et al.*, (1988, Fig. 10), are plotted here in Figure 15. These profiles have been obtained as follows. The vertical profiles observed by Peters *et al.* (1988) for eddy fluxes of respectively zonal momentum, meridional momentum and heat, are modeled quite realistically by

$$|J_{mx}| = 4 \times 10^{-2} F(z)\,\mathrm{N\,m^{-2}} \tag{22}$$

$$|J_{my}| = 1 \times 10^{-2} F(z)\,\mathrm{N\,m^{-2}} \tag{23}$$

$$|J_H| = 80 F(z)\,\mathrm{W\,m^{-2}} \tag{24}$$

where the form factor $F(z)$ is

$$F(z) = \frac{1 - \tanh\left(\frac{z-50}{20}\right)}{1 - \tanh\left(-\frac{50}{20}\right)}, \tag{25}$$

$z$ being measured in meters. The standard deviations $\sigma$ of the dynamical residuals are assumed 100% of the flux divergences:

$$\sigma\big(r_u(z), r_v(z), r_T(z)\big) = \left(\rho^{-1}\left|\frac{\partial J_{mx}}{\partial z}\right|, \rho^{-1}\left|\frac{\partial J_{my}}{\partial z}\right|, (\rho C_p)^{-1}\left|\frac{\partial J_H}{\partial z}\right|\right) \tag{26}$$

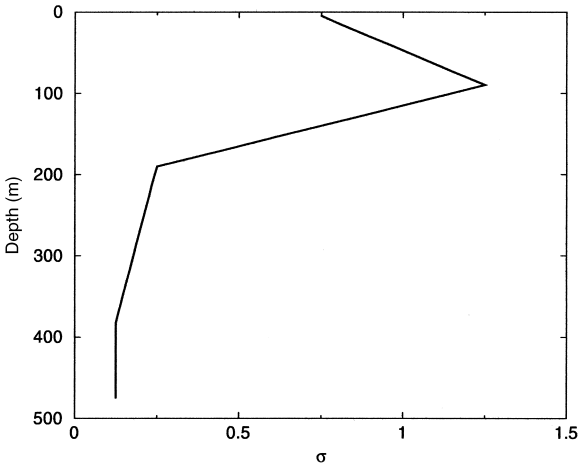


Figure 14. Vertical profile of the standard deviation of temperature, according to TAO climatology (units for σ: K).

with $\rho = 10^3\,\mathrm{kg\,m^{-3}}$ and $C_p = 4 \times 10^3\,\mathrm{J\,kg^{-1}\,K^{-1}}$. To clarify, subgridscale stresses are parameterized here using the KPP-interior scheme for diffusivities dependent upon local Richardson numbers (Large *et al.*, 1994); it is assumed that the errors in the divergences of these flux parameterizations are as large as the divergences of the actual turbulent stresses observed by Peters *et al.* (1988). It has been found that the heat flux divergence errors must be much larger than actual flux observations if the TAO subsurface temperature data are to be fit; the dashed line in Figure 15 is the enhanced magnitude, rather than the observed flux divergence profile.

The horizontal eddy flux of total thickness is parameterized with an eddy diffusivity $A_h = 1.25 \times 10^3\,\mathrm{m^2\,s^{-1}}$. Assuming a thickness variation of 20 m over a length scale of $2.5 \times 10^5$ m yields a diffusive rate of change of thickness of $4 \times 10^{-7}\,\mathrm{m\,s^{-1}}$. The standard error in this parameterization should be assumed to be 100 %, that is, the standard deviation of the thickness residual $r_h$ should be set at $4 \times 10^{-7}\,\mathrm{m\,s^{-1}}$.

The vertical correlations of all the initial residuals and dynamical residuals are assumed to be 'white', that is, errors at different discrete $s$-levels are assumed to be uncorrelated; for example,

$$C_s(s_n, s_m) = \delta_{n,m}. \tag{27}$$

*Surface fluxes*

The Gent–Cane model is driven by surface fluxes of momentum and heat. The priors of the momentum fluxes (pseudo stresses) are monthly-mean FSU archived values (Legler and O'Brien, 1988); priors for the heat fluxes are monthly-mean NCEP/NCAR reanalyses (Kalnay *et al.*, 1996). The standard deviations in the errors of these fluxes we estimated from

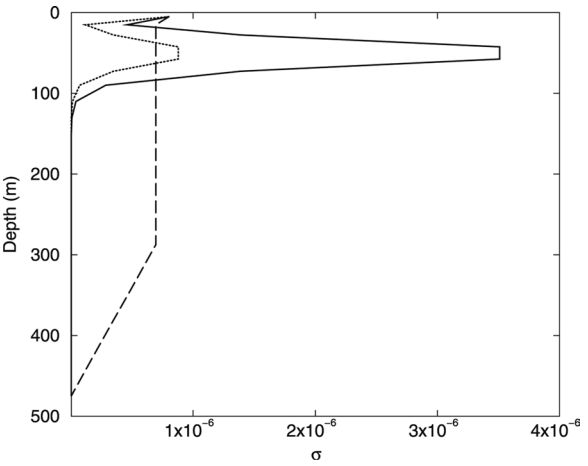


Figure 15. Vertical profile of observed eddy flux divergences. Solid line: zonal momentum, m s$^{-2}$. Dotted line: meridional momentum, m s$^{-2}$. Dashed line: heat, K s$^{-1}$ (enhanced).

the scales of the NCEP/NCAR reanalyses of winds and heat fluxes. Specifically, momentum flux errors $\delta q$ were estimated from wind errors $\delta \mathbf{u}_a$ by

$$\delta q = \rho_a C_D |\delta \mathbf{u}_a|^2. \tag{28}$$

With an air density $\rho_a = 1.2\,\mathrm{kg\,m^{-3}}$, a drag coefficient $C_D = 1.67 \times 10^{-3}$ and $|\delta \mathbf{u}_a| = 2\,\mathrm{m\,s^{-1}}$, (28) yields $\delta q = 8 \times 10^{-3}\,\mathrm{kg\,m^{-2}\,s^{-1}}$. Distributing these fluxes over a 10 m thick upper oceanic layer of density $10^3\,\mathrm{kg\,m^{-3}}$, the standard error of acceleration in the upper layer is $8 \times 10^{-7}\,\mathrm{m\,s^{-2}}$. A somewhat larger estimate would be obtained by replacing $|\delta \mathbf{u}_a|^2$ in (28) with $U_a|\delta \mathbf{u}_a|$, with $U_a$ a mean wind speed around 5 m s$^{-1}$; indeed, the chosen estimate of surface stress error is somewhat smaller than our very pessimistic scale estimate of errors in the subsurface momentum fluxes. However, such a linearization of the pseudostress error is unconvincing. Nevertheless, experiments have been performed with larger priors for the surface stress error, and are described in Appendix D. The heat flux error is assumed to be $35\,\mathrm{W\,m^{-2}}$; distributed over the upper layer, this yields a standard error of temperature rise of, coincidentally, $8 \times 10^{-7}\,\mathrm{K\,s^{-1}}$. The horizontal decorrelation scales for the surface flux errors are also based on NCEP/NCAR reanalyses.

*Notes*

(1) It may be seen in Table 4 that some length scales are depth dependent. The covariances are separable because of the lack of vertical correlation: see (27).

(2) The horizontal decorrelation scales $L_x$, $L_y$ in Table 4 are the same as those assumed for the $2\frac{1}{2}$ reduced-gravity model inverted by Ngodock *et al.* (2000). The decorrelation

time $\tau$ is shorter here, since the higher vertical resolution here should better resolve internal gravity waves.

(3) All cross-correlations between different circulation variables are assumed to vanish.

**Composite covariances**

*Initial residuals*

The components of the initial residuals have covariances of the form

$$C^{uu}_{ii}(x', y', s_n, x'', y'', s_m) = \sigma^u_i(s_n)\sigma^u_i(s_m)\delta_{n,m}\sigma_y(y')\sigma_y(y'')C_y(y' - y'')C_x(x' - x''). \tag{29}$$

The initial standard deviations are listed in Table 5.

*Dynamical residuals*

The components of the dynamical residuals have covariances of the form

$$C^{uu}_{ff}(x', y', s_n, t', x'', y'', s_m, t'') = \sigma^u_f(s_n)\sigma^u_f(s_m)\delta_{n,m}\sigma_y(y')\sigma_y(y'') \times C_y(y' - y'')C_x(x' - x'')C_t(t' - t''). \tag{30}$$

## APPENDIX C

**Relaxation**

A relaxation effect is added to the Picard iterations on the forward model (3), of the form

$$\mathbf{D}_{n-1}\mathbf{U}_n = \mathbf{F} + \mathbf{f}_n + \lambda\nabla^2(\mathbf{U}_n - \mathbf{U}_{n-1}), \tag{31}$$

where $\mathbf{D}_{n-1}$ is a linear operator that depends upon the preceding iterate $\mathbf{U}_{n-1}$. There is a corresponding term in the adjoint equation:

$$\mathbf{D}^\dagger_{n-1}\mathbf{A}_n = \cdots + \lambda\nabla^2\mathbf{A}_n, \tag{32}$$

where the superscript dagger denotes the adjoint operator. The dependent variable is $\mathbf{A}_n$ is the adjoint variable, that is, a weighting of the dynamical residual $\mathbf{f}_n$. The ellipsis denotes impulsive terms arising from the measurement functionals (see e.g., Bennett, 2002). Note that the relaxation effect in (31) vanishes in the limit, but the adjoint remains in (32) as a 'ghost.' Thus the correct adjoint equation is not solved, and so the inversion is suboptimal. However, in the experiment reported here, the diffusive relaxation parameter $\lambda = 10^3\,\mathrm{m}^2\,\mathrm{s}^{-1}$, while the conventional horizontal diffusivity already included in the iterated dynamical operator $\mathbf{D}_{n-1}$ and in its adjoint is $10^5\,\mathrm{m}^2\,\mathrm{s}^{-1}$. Thus the suboptimality is very slight.

## APPENDIX D

### Alternative hypotheses

Increasing the hypothesized standard errors in the NCEP surface fluxes of heat and momentum, from $35\,\mathrm{W\,m^{-2}}$ and $8 \times 10^{-3}\,\mathrm{N\,m^{-1}}$ to the surface values of the standard errors in the subsurface fluxes (which were set equal to the actual fluxes of $80\,\mathrm{W\,m^{-2}}$ and $4 \times 10^{-2}\,\mathrm{N\,m^{-1}}$ observed by Peters *et al.*, 1988), leads to slightly better dynamical fits and data fits. However, the test statistic $\hat{\mathcal{J}}$ is still way too large.

Restoring the standard errors in the NCEP surface fluxes to their originally hypothesized values, and reducing their decorrelation scales from $3 \times 10^6\,\mathrm{m}$ to $10^6\,\mathrm{m}$ leads to a slightly worse fit. There are more degrees of freedom in the surface flux controls or inputs, but the original total variance is now distributed over these extra degrees of freedom. The dynamics acts as a low–pass filter and so passes mostly the larger-scale inputs. These have had their variance reduced, thus there are fewer effective degrees of freedom in the output, rather than more. There is not a useful definition of a variance spectrum for this inhomogeneous solution; were there one, the spectral shape would have become flatter but more importantly the spectral amplitude would have become lower.

## REFERENCES

Abramowitz, M. and I. A. Stegun. 1964. Handbook of Mathematical Functions, National Bureau of Standards, Washington D.C., 1046 pp.

Amodei, L. 1995. Solution approcheé pour un problème d'assimilation de donneés meteorologiques avec prise en compte de l'erreur de modèlè. Comptes Rendus de l'Academie des Sciences, *321*, Seŕie IIa, 1087–1094.

Bennett, A. F. 1992. Inverse Methods in Physical Oceanography, Cambridge University Press, NY, 347 pp.

——— 2002. Inverse Modeling of the Ocean and Atmosphere, Cambridge University Press, NY, 234 pp.

Bennett, A. F., B. S. Chua and L. M. Leslie. 1996. Generalized inversion of a global numerical weather prediction model. Meteorology and Atmospheric Physics, *60*, 165–178.

——— 1997. Generalized inversion of a global numerical weather prediction model, II: analysis and implementation. Meteorology and Atmospheric Physics, *62*, 129–140.

Bennett, A. F., B. S. Chua, D. E. Harrison and M. J. McPhaden. 1998. Generalized inversion of Tropical Atmosphere-Ocean (TAO) data and a coupled model of the tropical Pacific Ocean. J. Climate, *11*, 1768–1792.

——— 2000. Generalized inversion of Tropical Atmosphere-Ocean (TAO) data and a coupled model of the tropical Pacific Ocean. Part II: the 1995–96 La Nina and 1997–98 El Niño. J. Climate, *13*, 2770–2785.

Bennett, A. F. and P. C. McIntosh. 1982. Open ocean modeling as an inverse problem: tidal theory. J. Phys. Oceanogr., *12*, 1004–1018.

Bennett, A. F. and M. A. Thorburn. 1992. The generalized inverse of a nonlinear quasi-geostrophic ocean circulation model. J. Phys. Oceanogr., *22*, 213–230.

Bogden, P. S. 2001. The impact of model–error correlation on regional data assimilative models and their observational arrays. J. Mar. Res., *59*, 831–857.

Chelton, D. B., F. J. Wentz, C. L. Gentemann, R. A. de Szoeke and M. G. Schlax. 2000. Satellite microwave SST observations of transequatorial tropical instability waves. Geophys. Res. Lett., *27*, 1239–1242.

Chua, B. S. and A. F. Bennett. 2001. An inverse ocean modeling system. Ocean Model., *3*, 137–165.

Egbert, G. D. 1997. Tidal data inversion: interpolation and inference. Prog. Oceanogr., *40*, 53–80.

Egbert, G. D. and A. F. Bennett. 1996. Data assimilation methods for ocean tides, *in* Modern Approaches to Data Assimilation in Ocean Modeling, P. Malanotte-Rizzoli, ed., Elsevier Press, NY, 147–179.

Egbert, G. D., A. F. Bennett and M. G. G. Foreman. 1994. TOPEX/POSEIDON tides estimated using a global inverse method. J. Geophys. Res., *99*, 24,821–24,852.

Gent, P. R. 1991. The heat budget of the TOGA-COARE domain in an ocean model. J. Geophys. Res., *96*, 3323–3330.

Gent, P. R. and M. A. Cane. 1989. A reduced-gravity, primitive equation model of the upper equatorial ocean. J. Comput. Phys., *81*, 444–480.

Hackert, E. C., A. J. Busalacchi and R. Murtugudde. 2001. A wind comparison study using an ocean general circulation model for the 1997–1998 El Niño. J. Geophys. Res., *106*, 2345–2362.

Haidvogel, D. B. and A. Beckmann. 1999. Numerical Ocean Circulation Modeling, Imperial College Press, River Edge, NJ, 320 pp.

Harrison, D. E., W. S. Kessler and B. S. Giese. 1989. Ocean circulation model hindcasts of the 1982–83 El Niño: thermal variability along the ship–of–opportunity tracks. J. Phys. Oceanogr., *19*, 397–418.

Kalnay, E., M. Kanamitsu, R. Kistler, W. Collins, D. Deaven, L. Gandin, M. Iredell, S. Saha, G. White, J. Woollen, Y. Zhu, A. Leetmaa, B. Reynolds, M. Chelliah, W. Ebisuzaki, W. Higgins, J. Janowiak, K. C. Mo, C. Ropelewski and J. Wang. 1996. The NCEP/NCAR 40-year reanalysis project. Bull. Amer. Meteor. Soc., *77*, 437–471.

Kauffman, B. G. and P. R. Gent. 1999. The NCAR CSM Pacific Basin Model: Version 3.e, User's Guide. `http://www.cgd.ucar.edu/csm/models/ocn-pac/pac3.e/doc0.html`.

Kessler, W. S., M. C. Spillane, M. J. McPhaden and D. E. Harrison. 1996. Scales of variability in the equatorial Pacific inferred from the Tropical Atmosphere–Ocean buoy array. J. Climate, *9*, 2999–3024.

Lacarra, J. F. and O. Talagrand. 1988. Short-range evolution of small perturbations in a barotropic model. Tellus, *40A*, 81–95.

Lanczos, C. 1966. The Variational Principles of Mechanics, University of Toronto, Toronto, 347 pp.

Large, W. C., J. C. McWilliams and S. C. Doney. 1994. Ocean vertical mixing: A review and a model with nonlocal boundary parameterization. Rev. Geophys., *32*, 363–403.

LeDimet, F.-X., H.-E. Ngodock, B. Luong and J. Verron. 1997. Sensitivity analysis in variational assimilation. J. Met. Soc. Japan, *75*, 245–255.

Legler, D. M. and J. J. O'Brien. 1988. Tropical Pacific wind stress analysis for TOGA, IOC Time series of ocean measurements, IOC Technical Series 33, Volume 4, UNESCO.

McCarty, M. E., L. J. Mangum and M. J. McPhaden. 1997. Temperature errors in TAO data induced by mooring motion. NOAA Tech. Memo. ERL PMEL-108, Pacific Marine Environmental Laboratory, Seattle, WA, 68 pp.

McCreary, J. P. and Z. Yu. 1992. Equatorial dynamics in a $2\frac{1}{2}$-layer model. Prog. Oceanogr., *29*, 61–132.

McPhaden, M. J. 1995. The Tropical Atmosphere-Ocean array is completed. Bull. Amer. Meteor. Soc., *76*, 739–742.

——— 1999a. Genesis and evolution of the 1997–1998 El Niño. Science, *283*, 950–954.

——— 1999b. El Nino: the child prodigy of 1997–1998. Nature, *398*, 559–562.

Morss, R. E. and D. S. Battisti. 2004a. Evaluating observing requirements for ENSO prediction: experiments with an intermediate coupled model. J. Climate, *17*, 3057–3073.

——— 2004b. Designing efficient observing networks for ENSO prediction. J. Climate, *17*, 3074–3089.

Muccino, J. C. and A. F. Bennett. 2004. Initial–boundary compatibility for inverse regional models. Tellus, *56A*, 141–153.

Ngodock, H. E., B. S. Chua and A. F. Bennett. 2000. Generalized inverse of a reduced gravity primitive equation ocean model and tropical atmosphere-ocean data. Mon. Wea. Rev., *128*, 1757–1777.

Peters, H., M. C. Gregg and J. M. Toole. 1988. On the parameterization of equatorial turbulence. J. Geophys. Res., *93*, 1199–1218.

Philander, S. G. 1990. El Niño, La Niña, and the Southern Oscillation. Academic Press, San Diego, CA, 293 pp.

Philander, S. G. H. and A. D. Siegel. 1985. Simulation of El Niño of 1982–1983, *in* Coupled Ocean–Atmosphere Models, J. Nihoul, ed., Elsevier, 517–541.

Phillips, O. M. 1966. The Dynamics of the Upper Ocean, Cambridge University Press, Cambridge, 261 pp.

Soreide, N. N., D. C. McClurg, W. H. Zhu, M. J. McPhaden, D. W. Denbo, M. W. Denbo and M. W. Renton. 1996. World Wide Web access to real–time and historical data from the TAO array of moored buoys in the tropical Pacific Ocean: Updates for 1996, *in* Proceedings of the OCEANS 96 MTS/IEEE, Ft. Lauderdale, FL, September 23–26, 1996, 1354–1359.

Stommel, H. M. 1954. Why do our ideas about ocean circulation have such a peculiarly dream–like quality?, *in* Collected Works of Henry M. Stommel, Vol. 1, N. G. Hogg and R. X. Huang, eds. 1995, American Meteorological Society, Boston, MA, 380 pp.

——— 1989. Why we are oceanographers. Oceanography, *2*, 48–54.

Temam, R. 2001. Navier-Stokes Equations: Theory and Numerical Analysis. American Mathematical Society, Providence, RI, 408 pp.

Zebiak, S. E. and M. A. Cane. 1987. A model El Nino/Southern Oscillation. Mon. Wea. Rev., *128*, 1757–1777.

Received: *5 July, 2005;* revised: *18 October, 2005.*